


## Theoretical study of intrinsic defects in cubic silicon carbide 3C-SiC

Peter A. Schultz<sup>1</sup>,<sup>✉</sup> Renee M. Van Ginhoven,<sup>2</sup> and Arthur H. Edwards<sup>3</sup><sup>✉</sup>

<sup>1</sup>Sandia National Laboratories, Albuquerque, New Mexico 87185, USA

<sup>2</sup>Directed Energy Directorate, Air Force Research Laboratory, Kirtland AFB, New Mexico 87117, USA

<sup>3</sup>Space Vehicles Directorate, Air Force Research Laboratory, Kirtland AFB, New Mexico 87117, USA

 (Received 22 February 2021; revised 30 April 2021; accepted 3 May 2021; published 17 May 2021)

Using the local moment counter charge (LMCC) method to accurately represent the asymptotic electrostatic boundary conditions within density functional theory supercell calculations, we present a comprehensive analysis of the atomic structure and energy levels of point defects in cubic silicon carbide (3C-SiC). Finding that the classical long-range dielectric screening outside the supercell induced by a charged defect is a significant contributor to the total energy, we describe and validate a modified Jost screening model to evaluate this polarization energy. This leads to bulk-converged defect levels in finite size supercells. With the LMCC boundary conditions and a standard Perdew-Burke-Ernzerhof (PBE) exchange correlation functional, the computed defect level spectrum exhibits no band gap problem: the range of defect levels spans  $\sim 2.4$  eV, an effective defect band gap that agrees with the experimental band gap. Comparing with previous literature, our LMCC-PBE defect results are in consistent agreement with the hybrid-exchange functional results of Oda *et al.* [*J. Chem. Phys.* **139**, 124707 (2013)] rather than their PBE results. The difference with their PBE results is attributed to their use of a conventional jellium approximation rather than the more rigorous LMCC approach for handling charged supercell boundary conditions. The difference between standard DFT and hybrid functional results for defect levels lies not in a band gap problem but rather in solving a boundary condition problem. The LMCC-PBE entirely mitigates the effect of the band gap problem on defect levels. The more computationally economical PBE enables a systematic exploration of 3C-SiC defects, where, most notably, we find that the silicon vacancy undergoes Jahn-Teller-induced distortions from the previously assumed  $T_d$  symmetry, and that the divacancy, like the silicon vacancy, exhibits a site-shift bistability in  $p$ -type conditions.

DOI: [10.1103/PhysRevB.103.195202](https://doi.org/10.1103/PhysRevB.103.195202)

### I. INTRODUCTION

Silicon carbide is a wide band gap semiconductor and a candidate material for use in high-power, high-frequency electronics in extreme environments (such as space), where its higher breakdown fields and lesser sensitivity to radiation and thermal effects (cf. silicon) would provide significant advantages for high-temperature applications or in radiation environments [1]. Its native oxide (away from the immediate interface) is  $\alpha$ -SiO<sub>2</sub>, making it compatible with standard MOSFET technology. The quality of the interface is good enough that the channel can be inverted, enabling CMOS technologies. There are 30 polytypes, with band gaps that range from 2.3 (3C-SiC) to 3.3 eV (2H-SiC). While the 4H is the most common polymorph used in technological applications, doped 3C-SiC has become interesting for potential electronic applications, e.g., in solar cells [2].

An understanding of the structural and electronic properties of atomic defects in the lattice is important to achieving the potential of this class of materials. Given the importance that defects play in the performance of SiC in electronic devices, little has been definitively determined concerning the behavior of defects in most SiC polytypes. The 3C-SiC is arguably the simplest of the SiC polymorphs, and the characterization of intrinsic defects in 3C-SiC has been the subject of several computational studies using density functional

theory methods [3–13]. Even in this simplest of polymorphs, however, there has been surprisingly little agreement about defects and their transition levels in the gap, and a good understanding is lacking of the electronic structure of even the most basic defect, the neutral silicon vacancy [7,13–15]. Many of the very early studies, while insightful, were computationally constrained to very small supercell models and  $k$  samples, making the results prone to finite size errors, and methods to properly account for charged boundary conditions were just beginning to be developed [16], making it challenging to evaluate reliable formation energies of charged defects.

Oda, Zhang, and Weber [13] advanced beyond these early studies to use a larger, more-converged 216-atom supercell for selected defects in 3C-SiC (both types of single vacancies, and single interstitials), with both a conventional local functional and a hybrid exchange correlation functional. Noting that conventional DFT manifested a large underestimate of the band gap, they attributed the differences between their DFT and their hybrid functional results for defect levels to a band gap problem in the DFT, that was eliminated by tailoring the hybrid functional to give the experimental band gap [17]. The DFT and hybrid functionals gave very similar results in defect structure and electron density distribution, these proved nearly interchangeable, but the ensuing defect levels were very different, leading to their conclusion that overcoming

the band gap problem was essential to describe defects in SiC [13].

In the present work, we investigate importance of overcoming the boundary condition problem and finite size errors in supercell calculations for a broad set of defects in 3C-SiC: C and Si vacancies, interstitials, and antisites, as well as divacancies and diantisites. We use the local moment countercharge method (LMCC) method [18–20] that more accurately treats the asymptotic boundary conditions for charged defect supercell calculations than the conventional jellium method. In previous applications to silicon [20], CsI [21], and III-V's such as GaAs [22], defect levels computed with this approach have been shown to not be sensitive to a Kohn-Sham band gap problem [23] and provide predictive accuracy to within 0.1–0.2 eV compared to measured experimental defect levels [20,21,24]. In 3C-SiC, a lack of definitive experimental assignments of defects to defect levels prevents a similar experimental validation of defects. Instead, when the more rigorous boundary conditions are applied, and finite size errors are eliminated in converged larger supercells, the band gap problem is found to be absent; the bounds defined by the range of computed defect levels proves to give a very good estimate of the experimental band gap. These results show great qualitative and quantitative similarity to the levels computed with hybrid functionals [13], showing that it is overcoming the boundary condition problem and not a band gap problem that is crucial to describe defects in 3C-SiC. With the computational economy afforded by the conventional DFT functionals, we explore the large-supercell limits of defects in 3C-SiC and verify that these results are converged with supercell size, obtaining new insights into the mystery of the neutral silicon vacancy, and better resolve questions concerning near-band-edge states in the interstitial and other defects.

The paper continues in the next section with a description of the computational methods and details of the calculations. This is followed by an analysis of the long-range dielectric screening energy, and development of an analytic model to accurately evaluate its contribution to a charged defect's total energy. This electrostatic energy outside the volume of the supercell is shown to be quite large, as large or larger than a band gap, making the construction of an accurate screening model an essential aspect of a viable computational approach. We describe the development of an analytic modified Jost model and demonstrate its efficacy in achieving cell size convergence even with rather small supercells. The subsequent section discusses the collective defect level diagram for the 3C-SiC defects considered here, and illustrates the consistency of these defect levels with the experimental band gap. This is followed by a description of the results for individual defects, including discussion of cell-size convergence, and making comparisons to previous calculations (where available in the literature). We close with a brief discussion and a section to conclude.

## II. COMPUTATIONAL METHODS

### A. Computational details

In the DFT calculations, we use SEQUEST, a local orbital, pseudopotential, DFT code [25]. The pseudopotentials are

standard Hamann-type generalized norm-conserving pseudopotentials [26] cast in the original semilocal form. The wave function solutions are expanded as linear combination of carefully optimized (double-zeta plus polarization) atom-centered contracted-Gaussian basis sets, that have been demonstrated to give converged results in previous defects studies [20]. In calculations of vacancies, additional “floating orbitals” on a phantom atom placed at the vacated atomic site are included in the basis set to remove basis-set incompleteness errors.

For computation of benchmark bulk properties of the SiC polytypes, we use both local density approximation (LDA) [27] and generalized gradient approximation (GGA). Calculations of defect energies in SiC require a more accurate treatment of spin polarization than offered by a local density approximation (LDA), thus we adopt the Perdew-Becke-Ernzerhof (PBE) flavor of the GGA [28] as the principal exchange-correlation functional used in the defect calculations, including spin polarization. The PBE functional does not incorporate the exact exchange that a hybrid functional does, but as shown below, this does not lead to materially different results once finite size errors are properly accounted for. The PBE calculations retain the computational economy of standard DFT, lose no meaningful accuracy in the description of the electronic structure with respect to hybrid functionals, and, using the efficient local-orbital basis, allow routine exploration of much larger unit cells that make possible the systematic elimination of finite size errors.

For the 3C-SiC defect calculations, we install a single defect into supercells that are  $2 \times 2 \times 2$ ,  $3 \times 3 \times 3$ ,  $4 \times 4 \times 4$ , and  $5 \times 5 \times 5$ , expansions of the conventional eight-atom cubic unit cell, computational models with 64, 216, 512, and 1000 atoms in the perfect crystal supercell, respectively. The Brillouin zone is sampled with a uniform  $3^3$   $k$  grid (offset from  $\Gamma$ ) in the 64-atom supercell, and a  $2^3$   $k$  grid is sufficient to converge the calculations for the larger supercells.

The lattice constants are fixed to the stress-optimized values computed for the perfect crystal, e.g.,  $a_0 = 4.388 \text{ \AA}$  for 3C-SiC with the PBE functional. The atomic positions are optimized until the force on each atom is less than 0.0003 Rydberg/Bohr ( $\sim 0.008 \text{ eV/\AA}$ ), found to be sufficient to converge a defect structure to less than 0.01 eV.

The state occupations across the defects are set to be consistent with occupations for an asymptotically dilute defect in a discrete defect occupation approach [20]. The Kohn-Sham levels of valid localized defect states are distinct from the band edge, and therefore there is no need for a finite “smearing” of states such as commonly used for metallic systems. The effective electronic temperature is set to zero. The ability to discriminate the Kohn-Sham state from the band edge markers in the supercell, assessed over a series of different supercell sizes, is the distinguishing characteristic used to discriminate a localized defect state [29]. However, the separation between a Kohn-Sham defect state and Kohn-Sham band edge marker has no role in determining the charge-transition defect level. The defect energy for charged systems is instead determined through a total energy method that includes rigorous treatment of electrostatic boundary conditions for a net charge in a periodic supercell.

To provide a more rigorous treatment of the electrostatic boundary conditions in supercell calculations of defects with net charge, we use the local moment counter charge (LMCC) method [18,19]. Unlike the conventional expedient of a jellium approach (using a flat background charge to neutralized a supercell), the LMCC method divides the charge into a model localized charge and a remainder neutral density, solving the Poisson equation for the model charge using Dirichlet boundary conditions that provide the correct  $q/r$  asymptotic behavior around an isolated charge and does not corrupt the potential in periodic images of the supercell, and for the remainder net-neutral charge using the usual periodic boundary conditions. The LMCC explicitly avoids the numerical divergence that accompanies supercell calculations of a periodic replicated net charge, and provides the correct asymptotic  $\frac{q}{r}$  electrostatic potential generated by an isolated charge in infinite bulk. This self-consistently induces the correct electron screening behavior near a charged defect within a finite supercell model [30] in response to that potential.

The LMCC identifies a fixed energy electron reservoir for net charge, formally equivalent to having the  $\frac{q}{r}$  potential for a net charge and the perfect crystal asymptotically align, at a distance infinitely far from the position of the defect—the bulk equivalent [19] of aligning to a vacuum level at zero for a molecular calculation [18]. The resulting shift from the defect cell average potential reference to the perfect crystal potential reference [19]  $E_{\text{defect}}^{\mu_e(q)}$  then allows electron removal and addition energies, ionization potential and electron affinity, to be computed with reference to the fixed electron reservoir.

That a well-defined electron potential reservoir energy is identified and enforced through the LMCC replaces the standard realignment of each defect calculation through a Kohn-Sham edge. The challenge of constructing a valid DFT defect energy changes, from this *ad hoc* realignment, to a meticulous and accurate description of finite cell contributions to the energy, and, especially, depends upon an accurate evaluation of the energy of dielectric screening outside the volume of the supercell.

The energy computed in a supercell DFT calculation of a defect with net charge  $q$  lacks long-range screening. For the evaluation of long-range classical screening contribution  $E_{\text{pol}}(q)$  to defect energy we use a modified Jost model [20,31]

(Rydberg atomic units):

$$E_{\text{pol}}(q; \text{cell}) = \left(1 - \frac{1}{\epsilon_0}\right) \left(\frac{q^2}{R_{\text{Jost}}^{\text{cell}}}\right). \quad (1)$$

This approximates the missing long-range screening energy outside the volume of a finite supercell by the classical dielectric screening response outside a sphere of radius  $R_{\text{Jost}}$  centered at a charge  $q$ .

The static dielectric constant  $\epsilon_0$  defining the isotropic dielectric medium in Eq. (1) is set to the experimental value (9.7) [32]. The final defect energy analysis proves only weakly sensitive to  $\epsilon_0$  of this magnitude. A computed GGA-PBE value for 3C-SiC (10.3) [17] lies within this range where the analysis is weakly sensitive.

The computed defect supercell energy, augmented by this long-range polarization becomes:

$$E_{\text{defect}}(q; \text{cell}) = E_{\text{cell}}(q) + E_{\text{defect}}^{\mu_e}(q) + E_{\text{pol}}(q; R_{\text{Jost}}^{\text{cell}}). \quad (2)$$

Note that this energy expression does not include any alignment to a band edge, it is strictly a ground state DFT that has incorporated long-range electrostatics. The first term is the raw energy reported from the calculation, the second term shifts the electrostatic reference to align with the perfect crystal density and potential, and the last addition adds the long-range screening energy that is not included within a finite size supercell

This approach provides the framework that has been validated to provide predictive 0.1 eV accuracy over dozens of defect levels in silicon [20]. Similar demonstrated accuracy in GaAs [22] could be used to confidently assign previously misidentified levels [23] on the strength of the computed defect levels. It has been also used effectively to analyze N-vacancy defect level positions in SiC [33].

## B. Verification: bulk properties

Table I summarizes the structural properties for 3C-SiC obtained in this work. We benchmark our results against selected previous computational works [13,17,34–37] and to experimental values [38–41]. The computed structural properties are broadly consistent with previous DFT work, providing a verification of the methods used here.

TABLE I. Structural properties of 3C-SiC: lattice parameter  $a_0$ , heat of formation  $\Delta H_f$  (cf. elemental diamond structure reference), and elastic constants  $C_{11}$ ,  $C_{12}$ ,  $C_{44}$ , and bulk modulus,  $B$  (in GPa).

Reference:	LDA			PBE				HSE	Exp.
	Current	[34]	[35]	Current	[36]	[37]	[17]	[17]	[38] <sup>a</sup> , [39]
$a_0(\text{\AA})$	4.327	4.315	4.34	4.388	4.38	4.380	4.379	4.347	4.3577 <sup>b</sup>
$\Delta H_f(\text{eV/f.u.})$	0.49	-	-	0.41	0.42	-	0.54 <sup>c</sup>	0.63 <sup>c</sup>	0.7 <sup>d</sup>
$C_{11}$	402	420	390	378	394	382	383	418	390, 395
$C_{12}$	135	126	134	120	133	128	127	141	142, 123
$C_{44}$	247	287	253	234	247	239	241	263	256, 236
$B$	224	223	222	206	220	213	212	233	225, 214

<sup>a</sup>As converted by Ref. [34].

<sup>b</sup>Reference [40].

<sup>c</sup>Reference [13].

<sup>d</sup>Reference [41] (using a graphite C reference).

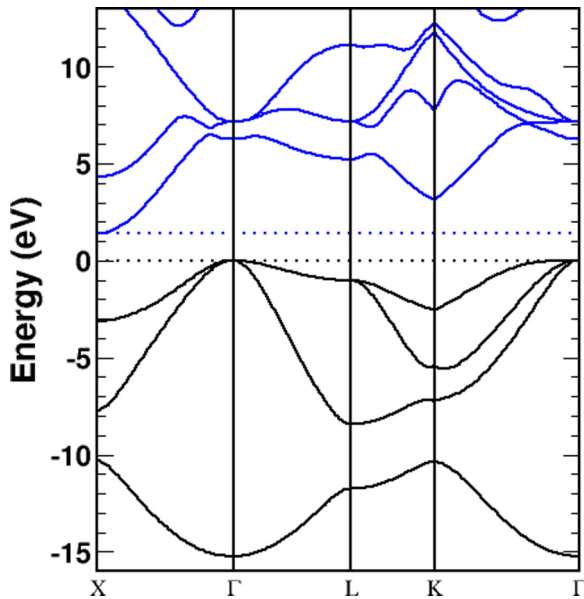


FIG. 1. Computed PBE band structure of SiC-3C using the local orbital basis and norm-conserving pseudopotentials. The valence band and conduction band edge positions are denoted by dotted lines, with the VBE aligned to 0.

These results are also in broad agreement with experimental measurements, validating that this computational context gives reasonable results for bulk SiC properties. The LDA and PBE results bracket the experimental lattice constant [40], both within 1%, typical behavior for local DFT. These results also roughly bracket the elastic constants, providing results to within 10% of the experimental values, the LDA stiffer and the PBE softer, again in line with the standard behavior and accuracy in these local functionals.

Figure 1 presents the computed PBE band structure. Compared to previous plane-wave-basis band structure calculations [17,42], these results demonstrate that our well-converged local orbital basis sets achieve excellent agreement not only for the occupied valence bands but several eV above the band gap into the empty conduction band states.

Table II summarizes the most important aspect of the band structure for prospective defect calculations, the width of the Kohn-Sham (KS) band gap, as computed here and compared to selected DFT literature and to experiment. The KS band gaps using these local functionals, at 1.3–1.4 eV, are observed to be much smaller than the experimental 2.417 eV [43] band gap for 3C-SiC. The empirically tuned HSE0.15 functional produced a Kohn-Sham gap that nearly matched the experimental band gap [17]. A formally more rigorous *GW* approach to

TABLE II. Kohn-Sham band gaps for 3C-SiC (eV). All band gaps are indirect  $\Gamma \rightarrow X$ .

Experiment: 2.417 eV (Ref. [43])				
LDA	Current	Ref. [44]	Ref. [35]	Ref. [45]
	1.326	1.24	1.30	1.30
PBE	Current	Ref. [17]	HSE/Ref. [17]	<i>GW</i> /Ref. [12]
	1.380	1.37	2.38	2.19

compute the band gap directly (as opposed to comparing KS levels) falls short by  $\sim 0.2$  eV. As we had demonstrated earlier in Si [20] and GaAs [23], we shall show below that mismatch between the smaller KS gap and the fundamental electronic band gap, infamously known as the “band gap” problem, is no impediment to defect level calculations across the full fundamental band gap.

### III. ANALYSIS OF LONG-RANGE SCREENING

It is not commonly appreciated in literature how significant classical long-range screening outside the volume of the computational supercell is to the energy of a charged defect. In Eq. (1), the long-range screening energy can amount to 1-10’s eV for typical size supercells and potentially accessible defect charge states. This energy dwarfs other energy scales in defect calculations; in particular, it is larger than typical band gap energies, which define the pertinent energy scale for defect levels. Given the importance of this classical long-range screening to the energy of a charge defect, we describe in greater detail the conceptual design of this screening, the implementation to determine the physical parameters defining the screening model, and then the verification of the long-range screening model for use in 3C-SiC.

The essential conceptual elements of the modified Jost screening model are illustrated in Fig. 2. An isolated defect with charge  $q$  in a semiconductor is screened by the infinite dielectric medium, Fig. 2(a). To make a tractable computational model in conventional DFT codes, a small region around the defect is excised and periodically replicated in a supercell approximation, Fig. 2(b). Assuming that the defect state itself is well-localized within the supercell (i.e., that the finite size errors become dominated by classical screening rather than quantum defect interactions) the supercell truncates the range of the screening included within a DFT supercell calculation. An exact accounting of the missing polarization energy outside a given supercell is impossible, the details of the edge and corner effects vary with the shape and size of the supercell, but it proves effective to estimate the missing screening energy by using an equivalent sphere, as in Fig. 2(c). The polarization energy due to a charge  $q$  outside of a sphere of radius  $R_{\text{Jost}}$  has an analytical solution in the Jost expression of Eq. (1).

In a naïve implementation, the  $R_{\text{Jost}}$  would be set to match the supercell volume,  $V_{\text{cell}} = \frac{4\pi}{3}R_{\text{Jost}}^3$ . However, the screening *inside* the supercell is by construction incomplete—the supercell construction fixes the electron count inside the supercell to be the full nominal charge  $q$  of the defect. The defect cannot be screened by the net polarization of electrons across a supercell boundary. As illustrated in Figs. 2(b) and 2(c), the outer boundaries of the supercell are descreened in order to screen the central region around the defect charge [30]. Hence to fully account for the missing long-range screening, long-range Jost dielectric screening term must be extended into this equivalent sphere volume by a skin depth  $R_{\text{skin}} = 1.1$  Bohr ( $\sim 0.6$  Å), as illustrated in Fig. 2(c),

$$R_{\text{Jost}} = R_{\text{cell}} - R_{\text{skin}} \quad (3)$$

and thereby recover the desired physical limit of a fully screened defect [Fig. 2(d)]. This physics-inspired correction can only be empirically determined, as described below, and



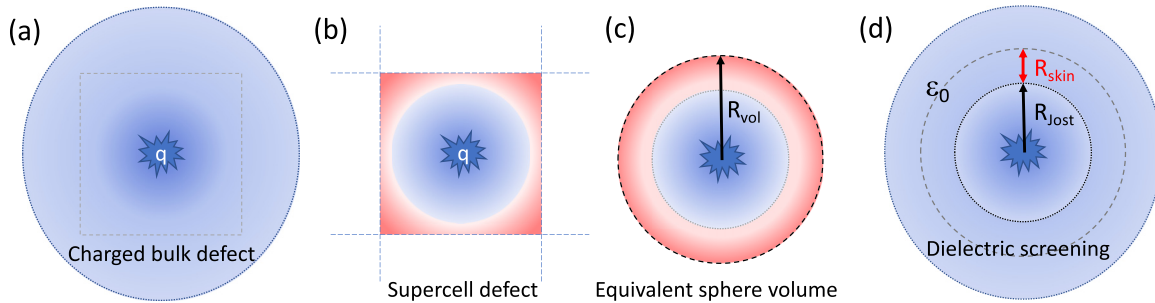


FIG. 2. A schematic diagram illustrating the evaluation of long-range screening energy contribution to a DFT supercell calculation of a charged defect. (a) The bulk defect with charge  $q$  has dielectric screening extending infinitely, inscribed square indicating the range of computational supercell. (b) The DFT supercell confines the full net charge  $q$  within the supercell parallelepiped, screening the near-defect region by drawing electrons from the supercell edges, descreening the edge region. (c) The equivalent-volume sphere, radius  $R_{\text{vol}}$ , around which long-range screening energy needs to be evaluated. (d) This radius is reduced by  $R_{\text{skin}}$  to account for the unscreened cell volume, leading to a Jost classical dielectric screening defined by  $R_{\text{Jost}}$ .

then must be verified in systematic cell-size extrapolation tests.

To calibrate the Jost model parameters, we select a single test defect, and examine the extrapolation behavior of its charge transition defect levels with Jost polarization. This Jost model, once calibrated with a single defect, is then used for all defects. In the 3C-SiC, we chose the silicon split-(110) interstitial as the calibration defect. The  $C_{2v}$  interstitial, while not the structural ground state for every charge state, has a stable localized charge state from the neutral defect through (4+). This offers the extrapolation behavior of multiple charge transitions to be simultaneously monitored, a built-in verification check. The existence of a (4+) offers a maximally stringent test of convergence, the energy incorporating a large Jost screening. The structure is relatively unchanged across the charge states, so differential relaxation effects between supercells are limited, allowing the extrapolation calibration to focus more exclusively on the electrostatic behavior rather than other finite size effects.

An ionization potential (IP) is computed in the usual way from the Jost-corrected defect energy in Eq. (4), as the difference between the energy of defects with different charges:

$$E_{\text{defect}}(q/(q-1); \text{cell}) = E_{\text{defect}}(q; \text{cell}) - E_{\text{defect}}(q-1; \text{cell}). \quad (4)$$

Note again, that this IP has still no alignment with any band edge, it is aligned with respect to the fixed LMCC-derived crystal potential.

For the interim purpose of extracting the screening-induced extrapolation behavior, we align the IP for all the charge transitions—the (1 + /2+), (2 + /3+), and (3 + /4+)—with respect to the (0/1+) transition. Figure 3 plots the IP for the  $\text{Si}_i$  charge transition energies from the smallest 64-site ( $2 \times 2 \times 2$ ) supercell through the largest 1000-site supercell, for different values of the Jost skin depth  $R_{\text{skin}}$ .

It is immediately apparent that the simple volume-matching sphere,  $R_{\text{skin}} = 0$  (marked with the red dotted lines), fails badly. In the 64-site cell (typical size used in many cost-limited hybrid functional approaches), this incurs an error  $\sim 0.2$  eV in the (1 + /2+) defect level level, and greater than 0.8 eV in the (3 + /4+) level. That error remains more than

0.1 eV in even the largest 1000-site supercell. This result indicates that simple scaling rules, such as that derived by Makov and Payne [16], need to be extended to include finite size effects—edge effects—in these very small supercells. Specifically, the need for an internal unscreened skin depth within each supercell would indicate an importance adding a term proportional to  $\frac{1}{L^2}$  in any practical dimensional analysis of finite size effects.

For each charge transition, each of the IP are seen to converge with supercell size, regardless of the screening model, to 0.33 eV below the (0/1+) for the (1 + /2+), 0.70 eV for the (2 + /3+), and 1.03 eV for the (3 + /4+) charge transition. With  $R_{\text{skin}} = 1.1$  Bohr ( $\sim 0.5$  Å), the IP converge to the asymptotic values within 0.01 eV for the 216-site supercell. The finite size errors are more significant in the

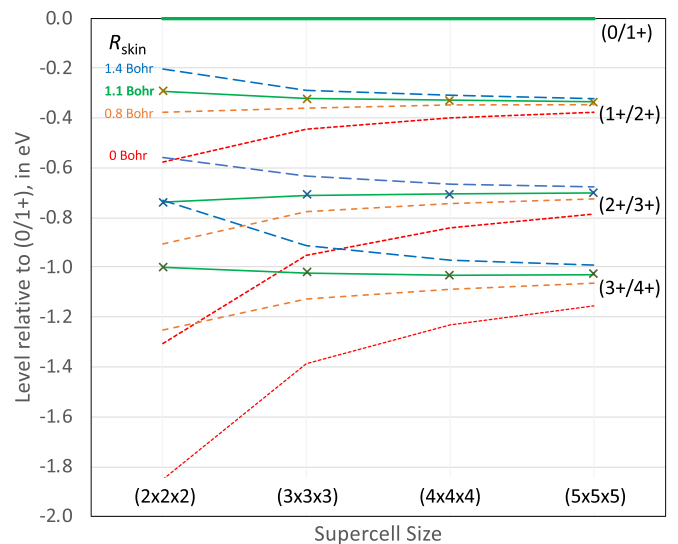


FIG. 3. Jost calibration using the  $\text{Si}_i$  test defect, from neutral to (4+) charge, all in the split-(110) structure without spin. Using a common  $R_{\text{skin}}$  unscreened skin depth of 1.1 Bohr ( $\sim 0.6$  Å) for all supercells, the computed relative defect levels from (0/1+) through (3 + /4+) all align across the supercells. Notably, the simple supercell-volume-matching sphere ( $R_{\text{skin}} = 0$ , dotted red lines) converges badly with cell size.

TABLE III. Classical long-range dielectric screening energy for 3C-SiC supercell sizes, for a defect of charge  $q$ , computed with the modified Jost approximation [Eq. (1)].

Supercell	Number of atoms	Jost polarization energy (eV)			
		$ q  = 1$	$ q  = 2$	$ q  = 3$	$ q  = 4$
$(2 \times 2 \times 2)$	64	1.328	5.312	11.952	21.248
$(3 \times 3 \times 3)$	216	0.851	3.405	7.662	13.622
$(4 \times 4 \times 4)$	512	0.627	2.506	5.639	10.024
$(5 \times 5 \times 5)$	1000	0.496	1.982	4.460	7.930

64-site supercell, but the Jost-screened IP calculated using the  $(2 \times 2 \times 2)$  supercell are nonetheless brought within 0.04 eV of the asymptotic IP. To appreciate the numerical precision of this convergence and the effectiveness of this modified-Jost screening, consider that this convergence in the 64-site supercell is resolved to within less than 0.2% of the computed Jost polarization contribution (21 eV) to the  $(4+)$  defect energy. Even in the 1000-atom supercell, the missing screening energy for  $q = 1$  is 0.5 eV, and for the  $q = 4$  is almost 8 eV.

Table III presents the long-range screening energy contribution to the defect energies, using this calibrated  $R_{\text{Jost}} = 1.1$  Bohr, for defects with charge up to  $|q| = 4$ , for the range of supercell sizes considered in these defect calculations. This modified-Jost model, calibrated using a single defect, is used in all charged defect calculations without any further modification. Its performance for other defects (presented below) can be used as additional verification of its accuracy.

The fine quantitative accuracy with which this modified Jost screening [Eqs. (1)–(3)] achieves its converged extrapolation is practical evidence of its validity. Its faithful expression of the nominal physical formulation depicted in Fig. 2 is conceptual evidence. This Jost expression uses the experimental dielectric constant, it does not need to be refit; this is an accurate description of the long-range screening. The optimal skin depth has the correct sign, to represent an unscreened region within the supercell, and has a reasonable magnitude, to represent a screening distance on the order of less than a bond length, consistent with analogous skin depths (i.e., correlated with lattice constant) determined in Si, GaAs, and other III-V semiconductors [20,22].

These cubic crystals lead to supercells that have Wigner-Seitz volumes that are roughly spatially isotropic, so that the mapping onto a spherical Jost model is a good representation of the missing screening, and one can straightforwardly use a series of supercells to calibrate and verify the modified Jost model. Other SiC polytypes, and hexagonal crystals (such as GaN) generally, supercells will not be conveniently isometric, so that a spherical Jost approximation will not be as appropriate. This makes a workable system in a hexagonal system less straightforward and more difficult to verify. However, one can carefully select supercells that are approximately isotropic in size that could be amenable to a spherical Jost correction. For example, for the  $(5 \times 5 \times 3)$  300-atom supercell in  $2H$ -SiC (wurtzite structure), the supercell  $\frac{c}{a}$  ratio is 1.015, an aspect ratio close enough to ideal to be amenable to a spherical Jost screening. This analysis and the corresponding results for hexagonal polymorphs will be reported elsewhere.

## IV. RESULTS

Table IV presents the computed PBE formation energies and ground state spin for the relaxed structures of an extensive set of intrinsic neutral defects in 3C-SiC: the simple silicon vacancy  $v_{\text{Si}}'$ , the site-shifted vacancy  $v_{\text{Si}}^*$  (forming a  $v_{\text{C}}\text{-C}_{\text{Si}}$  vacancy-antisite pair), the carbon vacancy  $v_{\text{C}}$ , the simple  $vv'$  and site-shifted  $vv^*$  divacancy, the carbon  $C_i$  and silicon  $\text{Si}_i$  interstitials, the single carbon  $\text{C}_{\text{Si}}$  and silicon  $\text{Si}_{\text{C}}$  antisites, and the  $\text{Si}_{\text{C}}\text{C}_{\text{Si}}$  di-antisite.

The formation energy  $E_{\text{form}}$  for the neutral defects is quoted in the Si-rich limit, evaluating

$$E_{\text{form}}[\text{defect}] = E_{\text{defect}}(\text{cell}) - n_{\text{Si}}\mu_{\text{Si}} - n_{\text{C}}\mu_{\text{C}}, \quad (5)$$

where  $E_{\text{defect}}(\text{cell})$  is the computed total energy of the supercell with the defect,  $n_{\text{Si}}$  and  $n_{\text{C}}$  are the number of Si and C atoms, respectively, in the defected supercell, and  $\mu_{\text{Si}}$  and  $\mu_{\text{C}}$  are the atomic chemical potentials. The formation energy of the perfect SiC crystal supercell is, by definition, zero, so that the sum of the silicon and carbon chemical potentials,  $\mu_{\text{Si}} + \mu_{\text{C}}$ , must exactly equal the energy of a formula unit in bulk 3C-SiC,  $E(3\text{C-SiC})$ . In the Si-rich limit, the chemical potential for the silicon  $\mu_{\text{Si}}$  is defined as the energy of Si in bulk Si, and the carbon chemical potential is determined as  $\mu_{\text{C}} = E(3\text{C-SiC}) - \mu_{\text{Si}}$ . We note that, with the knowledge of the SiC heat of formation  $\Delta H_f$  from bulk Si and bulk C (quoted in Table I), the Si-rich formation energy can be trivially converted to a C-bulk (or stoichiometric) limit [46].

Defect structures are concisely described, e.g., the  $C_i(0)$  ground state adopts a split- $(001)_{\text{C}}$  interstitial structure with  $D_{2d}$  symmetry. Where defects have multiple stable structures, they are listed separately. The simple Si vacancy has  $T_d$ -symmetric and distorted  $C_{3v}$  and  $C_{2v}$  structures. The silicon interstitial  $\text{Si}_i(0)$  has a stable  $T_{i(\text{C})}$  site (interstice with four C nearest neighbors), and a split- $(110)_{\text{Si}}$  interstitial configuration.

One immediate observation is the high propensity toward high-spin (triplet) ground states in SiC defects, in contrast to the low-spin tendency of defects in silicon or middle-row III-V's such as GaAs [22]. The dangling bonds of the first-row carbon atoms exposed in these often high-symmetry defects display strong exchange couplings. While our LDA results mostly capture these ground state structures, the prominence of spin polarization makes use of a GGA such as PBE more advisable, and we therefore proceed with a full set of results using PBE.

Dependence of formation energy on supercell size in neutral defects reflects finite size errors due to artificial

TABLE IV. Computed PBE neutral defect formation energies, in Si-rich limit (eV). A significant fraction of the defect structures have high-spin ground states. The predicted spin for each structure is either T (triplet) or S (singlet). Defect formation energies are determined as in Eq. (5). The notations for the defects and associated structure types is described in the text.

Defect	Structure	Spin	Supercell (number of atoms)				Ref. [13]	
			(2×2×2)	(3×3×3)	(4×4×4)	(5×5×5)	PBE	HSE
$v'_{\text{Si}}$	$T_d$	T	7.47	7.53	7.55	7.56	7.54	8.14
$v'_{\text{Si}}$	$C_{3v}$	T	<sup>a</sup>	7.30	7.30	7.30	-	-
$v'_{\text{Si}}$	$C_{2v}$	T	7.44	7.47	7.48	7.48	-	-
$v^*_{\text{Si}}$	$v_{\text{C}}C_{\text{Si}}-C_{3v}$	S	6.51	6.39	6.32	6.28	6.20	7.37
$v_{\text{C}}$	pair- $D_{2d}$	S	3.91	3.84	3.82	3.82	3.95	4.78
$vv'$	$C_{3v}$	T	7.14	7.16	7.17	7.17	-	-
$vv^*$	$v_{\text{C}}-C_{\text{Si}}-v_{\text{C}}-C_{2v}$	S	9.46	9.32	9.29	9.28	-	-
$C_i$	(001) $C-D_{2d}$	T	6.82	6.64	6.61	6.61	6.66	8.87
$\text{Si}_i$	$T_{i,C}-T_d$	T	10.04	8.84	8.67	8.60	8.10	9.84
$\text{Si}_i$	(110) $\text{Si}-C_{2v}$	S	8.83	8.56	8.51	8.51	8.24	9.43
$C_{\text{Si}}$	$T_d$	S	3.75	3.69	3.67	3.67	-	-
$\text{Si}_{\text{C}}$	$T_d$	S	3.51	3.37	3.34	3.34	-	-
$\text{Si}_{\text{C}}C_{\text{Si}}$	$C_{3v}$	S	5.16	5.09	5.08	5.07	-	-

<sup>a</sup>Corrupted electronic state collapses to  $T_d$ .

interactions with periodic defect images through confined elastic relaxation range [47] or electronic states corrupted by defect banding. Except for  $\text{Si}_i-T_{i,C}$ , the defect results in 512-atom supercells are fully converged to a bulk limit, closely matching the formation energies computed in 1000-atom supercells. The 216-atom supercell results are qualitatively similar, and still well converged to within about 0.1 eV. The results in the 64-atom supercells, in contrast, differ from larger supercell results by 0.2 eV or more, and in some cases are qualitatively wrong.

For the ground state Si vacancy, defect state banding in inadequately sized supercells gives a corrupted electronic state that collapses to a symmetric  $T_d$  structure rather than the actual  $C_{3v}$  structure cleanly favored in the larger supercells (by more than 0.2 eV). This is akin to the error that small supercells make in describing the neutral Si vacancy in silicon that favors the incorrect  $T_d$  symmetry rather than the actual  $D_{2d}$  ground state.

The Si interstitial  $\text{Si}_i-T_{i(C)}$  converges very badly with supercell size, and completely fails in the smallest 64-site supercell. This failure has yet another origin: the electronic states are very close to the conduction band edge (CBE) and cannot be unambiguously distinguished from a CBE state. These delocalized occupied states interact strongly across supercell boundaries.

This extrapolation study for just the neutral defect reveals that 64-site supercells are unreliable for studies of defects in a wide-gap semiconductor such as SiC. Supercells with 512 site sites are (mostly) converged, while 216-site supercells should be adequate except for edge cases that should be examined more closely. In Table IV, defect energies extracted from Oda *et al.* [13], using PBE and HSE are also listed. The good agreement with their PBE results for this selection of (neutral) defects (excepting the problematic  $\text{Si}_i-T_{i,C}$ ), is again confirmation that the local orbital basis here gives a representation of defect properties comparable to a highly converged, plane-wave basis, separated from the more contentious and

complicated issues associated with charge boundary conditions and the band gap problem.

#### A. Charged defect spectrum and effective defect band gap

Before we discuss the detailed features of individual defects, we present the full defect level spectrum, assembled from a full set of size-converged calculations, including all defect charged states that yield localized levels in the band gap. We show this set of computed thermodynamic levels for all the defects in Fig. 4. This level diagram distinguishes between the simple silicon vacancy and its site-shifted counterpart (C antisite-C vacancy pair) but otherwise ignores any barriers between different configurations of other bistable defects (divacancy, Si interstitial) that might impede observing a given transition in a thermal measurement such as DLTS. These defect levels are obtained by taking total energy differences between the fully relaxed lowest energy structure for each defect in each charge state, each verified to arise from a defect calculation with the Fermi level in the KS band gap, i.e., localized eigenstates. Calculating the available charge states for each defect, using the methods described above to determine ionization potentials, leads to a set of levels in the band gap all defined relative to each other. When considered together, the collected thermodynamic levels define a minimum span of the effective defect band gap. We do not determine directly where the band edge is. It may be inferred by the identification of a shallow level (but not too shallow, as such levels may not be distinguished from the edges). For this set of calculations, the zero is set by aligning to the lowest clearly localized state, which in this case is the  $(4+ / 3+)$  silicon antisite defect level. The highest state shown in Fig. 4 is for  $v'_{\text{Si}}$ , at about 2.5 eV. This particular state is still not converged at 512 atoms, continues to fall in larger systems, while also showing increased interaction with conduction band states. We judge this is possibly not a valid charge state in these PBE calculations, but include it for completeness. The highest

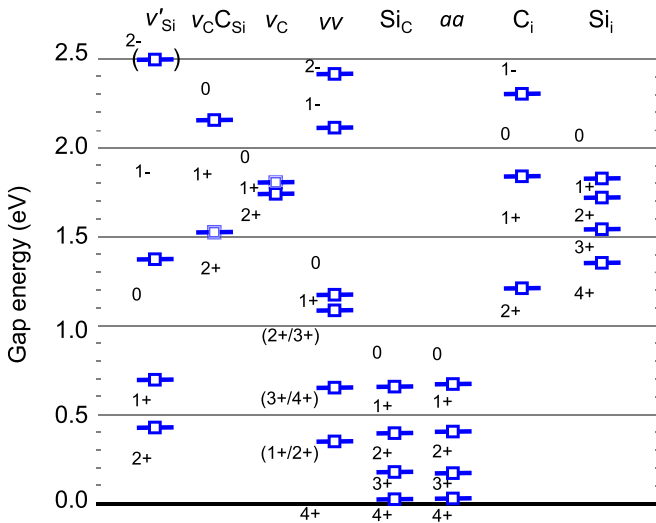


FIG. 4. Computed thermodynamic defect levels for 3C-SiC calculated using PBE functional and a total energy approach using the LMCC method for charged defects, extrapolated from the 512-site supercell results. From left to right, the defects are silicon vacancy (simple  $v'_{\text{Si}}$ , and site-shifted  $v_{\text{Si-C}_{\text{Si}}}$ ), carbon vacancy, divacancy, silicon antisite, the diantisite, carbon interstitial, and silicon interstitial. Each mark indicates the level where the system charge changes, and the expected defect charge is indicated by numbers between the predicted transition levels. For example, for the simple silicon vacancy  $v'_{\text{Si}}$ , the charge state is (2+) below a Fermi level of  $\sim 0.4$  eV, and changes at this level to be (1+) up to the next level at  $\sim 0.7$  eV. The effective zero (valence band edge) is aligned to the lowest clearly defined, well-localized defect level, in this case the (4+ / 3+) silicon antisite defect level. The rest of the spectrum is placed in relation to the effective zero, and together, the extent of the levels defines a minimum extent of the effective defect band gap. The  $v'_{\text{Si}}$  (2- / 1-) (in parenthesis) shows contamination by conduction band states with supercell size, and is likely not converged at 512 atoms. This is possibly not a valid charge state in these PBE calculations, but likely only marginally outside the gap, and thus included for completeness.

fully converged, well-defined charge state is the divacancy (vv) (2-). The full span of defect levels is just under 2.4 eV, right at the experimental band gap for this material.

Just as in the case of defect level diagrams in silicon [20], gallium arsenide [22], and in a CsI ionic crystal [21], generated with the LMCC method and a conventional local functional such as PBE, the defect levels computed in 3C-SiC with the PBE functional and presented in Fig. 4 are unhindered by a band gap problem and, indeed, span the full width of the experimental band gap.

The width of the effective defect band gap is not imposed, scaled, or otherwise fitted in these PBE calculations. Unlike a more empirical hybrid functional approach, which is fit to reproduce the experimental band gap [17], the width of the effective defect band gap is not predetermined in these PBE calculations. The band edges are not set by a KS band edge, but arise naturally as upper and lower bounds of the defect ionization potentials computed as total energy differences in Eq. (4).

A possible counterargument is that the expanded defect gap is the accidental consequence of an artificially inflated gap

TABLE V. Supercell band gaps.

Supercell (number of atoms)/ $k$ grid	LDA	PBE
$(2 \times 2 \times 2)$ [64]/ $3^2$	1.906	1.944
$(3 \times 3 \times 3)$ [216]/ $2^2$	1.906	1.944
$(4 \times 4 \times 4)$ [512]/ $2^2$	1.674	1.718
$(5 \times 5 \times 5)$ [1000]/ $2^2$	1.556	1.603
...	...	...
$\Gamma \rightarrow X$	1.326	1.380
Effective defect gap	( $\sim$ PBE) <sup>a</sup>	2.4
Experiment:	2.417 eV (Ref. [43])	

<sup>a</sup>The full defect series needed to identify the defect level bounds was not completed in the LDA, but the partial results show close similarity to the corresponding PBE results.

from performing the calculations in finite supercells and discrete  $k$  grids. The summary of the computational band gaps in Table V probes this notion. The  $(2 \times 2 \times 2)/3^2$  and  $(3 \times 3 \times 3)/2^2$  supercells, having formally equivalent  $k$  points, share the same supercell band gap, 1.9 eV. This shrinks to 1.7 eV in the  $(4 \times 4 \times 4)/2^2$  supercell and yet further to 1.6 eV in the  $(5 \times 5 \times 5)/2^2$  supercell. While larger than the PBE band gap (1.38 eV), these are all smaller than the computed effective defect band gap. Moreover, as will be shown below, most defect levels are mostly insensitive to the supercell size and the associated shrinking supercell KS gap. See Fig. S1 in Ref. [48] for the cell-size convergence of the full defect level diagram.

## B. Intrinsic defects

The details of each defect are presented in this section. Individual defect level figures are aligned to the level positions obtained from the full gap-spanning defect spectrum shown in Fig. 4.

### 1. Silicon vacancy - $v'_{\text{Si}}$

The silicon vacancy is the iconic defect of SiC, quite simple and well-understood in some respects, but thus far completely inscrutable in others. It is the subject of numerous experimental [49–51] and computational studies [5,7,8,11,13–15,52,53] that have yet to resolve very basic questions about the defect.

The  $v_{\text{Si}}$  in SiC was identified early to be metastable [52]. It adopts both a simple  $v'_{\text{Si}}$  and a site-shifted configuration  $v^*_{\text{Si}}$  as depicted in Fig. 5, where a neighboring C atom shifts to the

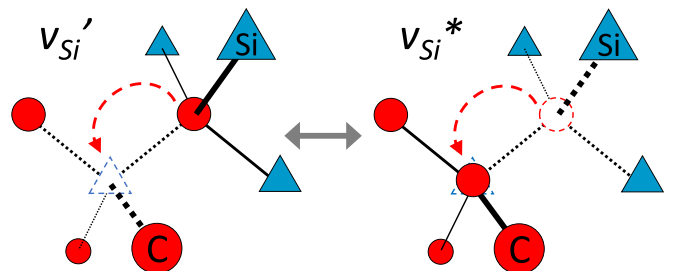


FIG. 5. Schematic depiction of the  $v_{\text{Si}}$  bistability between the simple vacancy  $v'_{\text{Si}}$  and site-shifted vacancy  $v^*_{\text{Si}}$  ( $= v_{\text{C}} C_{\text{Si}}$ ).



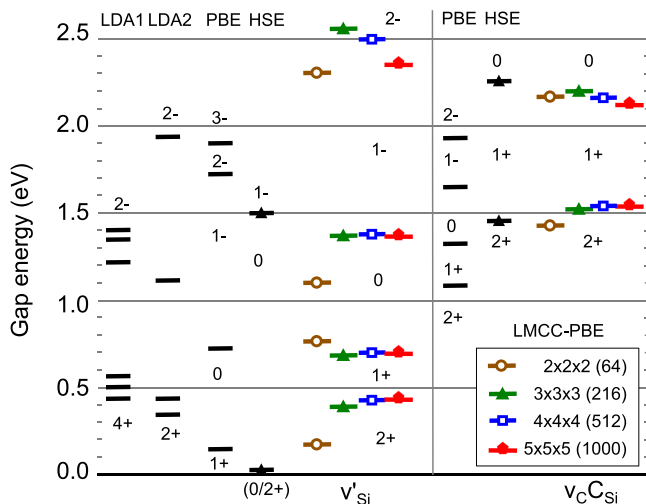


FIG. 6. The defect levels for the simple silicon vacancy,  $v'_{\text{Si}}$  (left) and site-shifted vacancy  $v^*_{\text{Si}}$  ( $= v_{\text{C}} C_{\text{Si}}$ ) (right). For  $v'_{\text{Si}}$ , results from left to right are: LDA using small systems from Torpo(LDA1) [14] and Zywiets(LDA2) [5], 216 atoms using PBE and HSE levels from Oda [13] (black lines and solid triangles) and the current results using LMCC-PBE for system sizes 64, 216, 512, and 1000 atoms, depicted using open brown circles, solid green triangles, open blue squares, and solid red pentagons, respectively. For  $v_{\text{C}} C_{\text{Si}}$ , Oda PBE and HSE, and the current LMCC-PBE results are shown. The charge states for each level are depicted as in Fig. 4. For the  $v'_{\text{Si}}$ , differences in the levels are due to both boundary conditions, and differing defect geometry. The LDA, PBE, and HSE results have a  $T_d$  ground state structure for all charge states. For LMCC, we have a sweep through differing ground state geometry with each charge. The geometry is  $T_d(2+) \rightarrow C_{2v}(1+) \rightarrow C_{3v}(0) \rightarrow T_d(1-)$ . At  $(2-)$ , the system remains at  $T_d$ . The quality of this higher charge state is questionable, showing differing levels of contamination with CB states that increases with supercell size. It is included to show the limits of the shallow band edge, marking the upper limit of the possible gap. The  $v^*_{\text{Si}}$  results show reasonable agreement with the HSE calculations.

vacated Si site to form a  $C_{\text{Si}}-v_{\text{C}}$  pair. We find the simple  $v'_{\text{Si}}$  adopts stable charge states from  $(2+)$  up to (almost?)  $(2-)$ , and the site-shifted  $v^*_{\text{Si}}$  takes stable charge states from  $(2+)$  to  $(0)$ . In GaAs, the  $v'$  and  $v^*$  was shown to interconvert with low barriers [24] motivating treating the metastability as a single defect. Computing such barriers is beyond the scope of this work, and is expected to exhibit complex behavior involving allowed spin transitions in concert with atomic motion and changing with the system fermi level. In addition, calculations from Bruneval and Roma [11] and Van Ginhoven [54] indicate large ( $>2\text{ eV}$ ) barriers for interconversion. Therefore in the current work, we present results for  $v'_{\text{Si}}$  and  $v^*_{\text{Si}}$  levels as separate defects in Fig. 6.

The  $v_{\text{Si}}(1-)$  is well-understood. Itoh *et al.*, observed a defect center in EPR (electron paramagnetic resonance)[49] they labeled  $T1$  with  $T_d$  symmetry, with a quartet spin state, and assigned to the symmetric  $T_d$   $v'_{\text{Si}}(1-)$ . In a symmetric  $T_d$  structure, the  $v'_{\text{Si}}$  exhibits a triply degenerate  $t_2$  state in the gap. In the  $(1-)$ , each of these is occupied by one electron, high-spin coupled in line with Hund's Rule, into a  $^4A_2$  ( $S = 3/2$ ) state, as shown in DFT calculations [14]. This assignment was

further bolstered by agreement of calculated hyperfine tensors [53] with the data. Our results agree, predicting a high-spin  $T_d(1-)$  ground state from the smallest 64-site to the largest 1000-site supercell.

Unambiguous characterization of other charge states of the vacancy, either in experiment and especially in computational modeling, has been more challenging. Adding or removing electrons from the  $(1-)$  would lead to a degenerate total ground state, where Jahn-Teller instability should trigger a structural distortion from the  $T_d$  to a lower energy structure that eliminates the degeneracy. Torpo *et al.* [14] did not find a distorted structure for any charge state of  $v'_{\text{Si}}$  nor did later computational studies [5,7,8]. This result was particularly perplexing for the neutral vacancy. The DFT results indicate a mid-gap range  $(1- / 0)$  level, indicating an ostensibly localized neutral defect, which should lead to a triplet-spin  $T_d$  structure that should be observable in experiment. Experiments showed no signs of this DFT-predicted structure [49,50].

Deak *et al.*, having anticipated, and not found, a  $D_{2d}$  distortion analogous to that seen for the vacancy in silicon, reasoned that a proper description of  $v'_{\text{Si}}(0)$  in the  $T_d$ -conserving structure would be indescribable within the one-electron picture of DFT and require a multi-configurational description [7]. In a small cluster-based configuration interaction (CI) calculation, they determined that a singlet state ( $^1E$ ) would be 0.17 more stable than the high-spin triplet. Introducing a “mixed spin” approach, exploring anti-ferromagnetic spin configurations within a reduced  $D'_{2d}$  electronic symmetry (but within an ionic configuration and total electron density that remained  $T_d$ ), Zywiets *et al.* [15] also found a  $S = 0$  state to be lower than the high-spin triplet, by 0.02 eV in LDA and 0.06 eV in GGA. Oda *et al.* expanded upon this analysis to more general spin configurations and other charge states and found a mixed-spin  $S = 0$  state to be 0.22 and 0.07 eV lower than the high-spin  $T_d$  triplet state using PBE, and HSE, respectively [13].

We find a distorted  $C_{3v}$  structure to be the ground state for the neutral  $v'_{\text{Si}}$ . This is a conventional (for DFT) triplet-spin structural distortion that eliminates the Jahn-Teller degeneracy in the  $T_d$  symmetry. As shown in Table IV, this distorted triplet-spin  $C_{3v}$  structure is 0.26 eV below the  $T_d$  triplet state, a margin that surpasses energy lowering computed for the singlet- $T_d$  in either the CI [7] or mixed-spin DFT [5,13] calculations. This result indicates the dominance of exchange coupling among the carbon dangling bonds of the defect and favors a high-spin triplet over these singlet-spin candidates as the ground state.

The  $L3$  center observed in ODMR (optically detected magnetic resonance) was a triplet-spin,  $C_{3v}$  defect and believed to be  $v_{\text{Si}}$ -involved. While plausible to assign this  $C_{3v}$  symmetry defect to this experimental defect center and thereby resolve the mystery of the missing  $v_{\text{Si}}(0)$ , the differing annealing behavior observed for the  $T1 = v_{\text{Si}}(1-)$  EPR center [49] and the  $L3$  ODMR center [50] leads to caution in making this assignment.

This unexpected (after so many previous studies) result requires explanation. A rationalization comes from the failure to obtain a localized  $C_{3v}(0)$  in the 64-site cell. Such a highly localized state (as evidenced by the near-perfect convergence in larger supercells) would be expected to manifest also in the

smaller 64-atom cell. It does not because of finite cell errors. The defect banding is large enough to overwhelm the degeneracy splitting induced by the lowered symmetry. The electronic KS state is corrupted as a mixed orbital state, the averaged occupations cause a collapse to the symmetric  $T_d$  structure. This misbehavior would be exacerbated by the conventional practice of using an artificial electronic temperature in DFT calculations (our calculations are  $T = 0$ ). This smearing tends to reduce differentiation between the three  $t_2$ -descended state occupations, biasing toward a  $T_d$  description with equal occupations. Early studies involved small  $O(100)$  supercells were not able to isolate a stable  $C_{3v}$ , and later studies emphasized what was deemed a more plausible  $D_{2d}$  distortion instead [7,15].

As presented in Table IV, a triplet-spin  $C_{2v}$  distortion also results in lower energy, although not as low as the  $C_{3v}$ . We were unable to find a significant  $D_{2d}$  distortion from the  $v_{\text{Si}}(0)$ , significant being defined as the  $\sim 0.01$  eV practical resolution to differentiate defects within the DFT calculations. This reproduces the earlier results concerning the stability of the  $D_{2d}$  [7,14,15].

The  $T_d$  and  $C_{3v}$  lie on different DFT potential energy surfaces. The ground state configuration in the  $T_d(0)$  has an averaged  $2/3$  electron occupation in each of the three degenerate  $t_2$  orbitals:  $t_{2,x}^{2/3} t_{2,y}^{2/3} t_{2,z}^{2/3}$ . Projecting up to the  $T_d$  symmetry, the ground state configuration for the  $C_{3v}$  maps to  $e^\uparrow e^\uparrow a_{111}^0 \rightarrow t_{2,x}^\uparrow t_{2,y}^\uparrow t_{2,z}^0$  (rotating the  $t_2$  basis to orient one of them along the 111 axis). Leaving aside that the average occupations in the  $T_d$  structure leads to an improper mixed state while the  $C_{3v}$  structure provides a proper single-electron, integer-electron-per-orbital state, the important difference lies in the spin density distribution produced by these different electronic configurations. The  $T_d$  structure (and, incidentally, the symmetry-reduced  $D_{2d}$  structure) distributes the spin density equally over all four neighboring carbon atoms. In the  $C_{3v}$ , the triplet coupled electrons occupy degenerate  $e$  orbitals with a node along the (111) axis. The spin density is distributed over only three carbon centers. This strengthens the exchange coupling between the electrons, resulting in a larger spin polarization from the more localized electronic spin density.

The spin doublet  $v'_{\text{Si}}(1+)$  also undergoes a Jahn-Teller distortion in these calculations, to a  $C_{2v}$  structure that is  $>0.1$  eV lower than the  $T_d$ . This distortion strengthens with increasing cell size, confirming its stability,

We could not isolate any stable distortion in the  $v'_{\text{Si}}(2-)$ . Given the presence of the level right at the band edge (Fig. 6), this additional electron is very delocalized at best, and unable to drive a significant distortion. The calculations indicate contamination with the CBE, a hybridization increasing with larger supercells. We judge this is possibly not a valid charge state in these PBE calculations, but likely only marginally outside the gap.

The site-shifted  $v^*$  is far lower energy for all of its stable charge states. The  $v^*(0)$  is already almost hybridized with the CBE, so no  $v^*(1-)$  exists. The  $v^*(0)$  is 1.0 eV more stable than  $v'(0)$ , the  $(1+)$  more stable by more than 2.4 eV and the  $(2+)$  by more than 3.5 eV. In  $p$ -type SiC, the site shift will dominate and the simple vacancy will occur only in negligible populations.

The defect levels constrained to the site-shift structure are 1.5 eV above the VBE for  $(2+/1+)$  and  $\gtrsim 2.1$  eV for  $(1+/0)$ . These differ greatly from earlier PBE defect levels [13], but instead are in good agreement with the HSE hybrid functional defect levels presented by Oda *et al.*, as illustrated in Fig. 6. That the quoted PBE levels differ can be directly attributed to the use of a more rigorous LMCC-based treatment of the charge boundary conditions in the current work. It is intriguing that the HSE results obtain similar results as the LMCC-PBE, despite the lack of proper control of the charge boundary conditions in the HSE.

Considering the  $v'_{\text{Si}}$  and  $v^*_{\text{Si}}$  as a single defect, the  $v_{\text{Si}}(0)$  is not thermodynamically stable for any position of the Fermi level in the gap. The stability jumps from  $v'_{\text{Si}}(1-)$  to  $v^*_{\text{Si}}(1+)$  in what would be a  $-U(1-/1+)$  transition. Such an electronic transition is unlikely to be activated at reasonable temperatures due to the predicted large barriers for the site shift in 3C-SiC.

Figure 6 displays the defect levels for the simple silicon vacancy,  $v'_{\text{Si}}$  and site-shifted vacancy  $v^*_{\text{Si}}$  ( $= v_{\text{C}}C_{\text{Si}}$ ) as compared to corresponding previous studies using LDA [5,14] and PBE/HSE [13]. The LMCC results plainly demonstrate the need for larger supercells to reliably predict the charged states of this defect. These differences are due to both the boundary conditions, and also the different (distorted) defect geometries. For the  $v'_{\text{Si}}$ , differences in the levels are due to both boundary conditions, and differing defect geometry. The LDA, PBE, and HSE results have a  $T_d$  ground state structure for all charge states. For LMCC-PBE, we have a sweep through differing ground state geometry with each charge. Reading upwards with the number of electrons  $(2+) \rightarrow (1+) \rightarrow (0) \rightarrow (1-) \rightarrow (2-)$ , the geometry is  $T_d \rightarrow C_{2v} \rightarrow C_{3v} \rightarrow T_d$ . At  $(2-)$ , the system remains at  $T_d$ . As discussed above, the quality of this  $(2-)$  state is questionable, showing differing levels of contamination with CB states that increases with supercell size. It is included to show the limits of the shallow band, marking the upper limit of the possible gap. On the other hand, the  $v^*_{\text{Si}}$ , with its clearly defined geometry and strong localization for all examined charge states, shows remarkable agreement between the jellium-HSE and our LMCC-PBE results.

## 2. Carbon vacancy - $v_{\text{C}}$

The immediate environment of the carbon vacancy in SiC is chemically equivalent to the silicon vacancy in silicon: a vacant site with four silicon nearest-neighbor atoms, each with an inward-directed dangling bond. As in elemental silicon, this neutral vacancy distorts to a paired- $D_{2d}$  structure, as does the positive vacancy, while the doubly ionized vacancy returns to the symmetric  $T_d$  structure.

As shown in Table VI, the neutral vacancy in SiC has a stronger distortion from a  $T_d$  to a pair- $D_{2d}$  than in Si. The cell-converged distortion energy  $\Delta E_f^{T_d}$  is roughly the same (0.4 eV), but the paired- $D_{2d}$  distortion dominates in even the small 64-site SiC supercell. In silicon, supercells are significantly more affected by finite-size errors, to the point that the 64-site system is so badly compromised that a  $D_{2d}$  structure cannot be isolated.

TABLE VI. Distortion parameters for 3C-SiC: $v_C$  (carbon vacancy in SiC) and Si: $v_{Si}$  (silicon vacancy in silicon).  $E_f^{D_{2d}}$  is the formation energy of the neutral  $D_{2d}$  ground state geometry.  $\Delta E_f^{T_d}$  is the difference in energy from the  $T_d$  geometry, the amount by which the  $D_{2d}$  is favored. The parameter  $c_t/a_t$  is a measure of tetragonal ( $D_{2d}$ ) distortion in the near neighbor atoms, as defined in Reference [29].  $R_{Si-Si}^{D_{2d}}$  and  $R_{Si-Si}^{T_d}$  are the distances between the nearest-neighbor silicon atoms adjacent to the vacancy site in SiC and pure Si, respectively.

	$E_f^{D_{2d}}$ (eV)	$\Delta E_f^{T_d}$ (eV)	$c_t/a_t$	$R_{Si-Si}^{D_{2d}}$ (Å)	$R_{Si-Si}^{T_d}$ (Å)
$v_C$ (3C-SiC)					
(2×2×2)	3.911	-0.39	1.244	2.782	3.117
(3×3×3)	3.841	-0.50	1.259	2.764	3.202
(4×4×4)	3.823	-0.45	1.265	2.758	3.258
(5×5×5)	3.822	-0.38	1.263	2.759	3.278
$v_{Si}$ (silicon)					
(2×2×2) <sup>a</sup>	3.619	-0.00	1.015	3.587	3.609
(3×3×3)	3.616	-0.17	1.306	3.069	3.505
(4×4×4)	3.595	-0.32	1.305	3.032	3.493
(5×5×5)	3.589	-0.41	1.309	3.021	3.494

<sup>a</sup>Collapses to  $T_d$  because of corrupted electronic state.

The  $D_{2d}$  tetragonal distortion ratio  $c_t/a_t$  [29] converges far from the  $T_d$  ideal value of 1. The SiC vacancy has shorter bonds for Si-Si pairs, as seen in  $R_{Si-Si}^{D_{2d}}$ , in part because the smaller SiC lattice starts with shorter Si-Si distances across a vacancy.

A comparison of electrical levels is shown in Fig. 7. In silicon, the  $D_{2d}(0) \rightarrow T_d(2+)$  structural rearrangement displays a negative- $U$  transition near the VBE edge [55], the (0/1+) defect level below the (1+/2+) charge transition. Early LDA studies [5,8,56] echoed this behavior in 3C-SiC, with  $-U$  ranging from 0.15 [8] to 0.31 eV [5,57]. More recent calculations [13] and our converged PBE results do not show  $-U$ , with the  $v_C(0/1+)$  level at VB + 1.81 eV being 0.06 eV above the  $v_C(1+/2+)$  level at 1.75 eV. We find that the

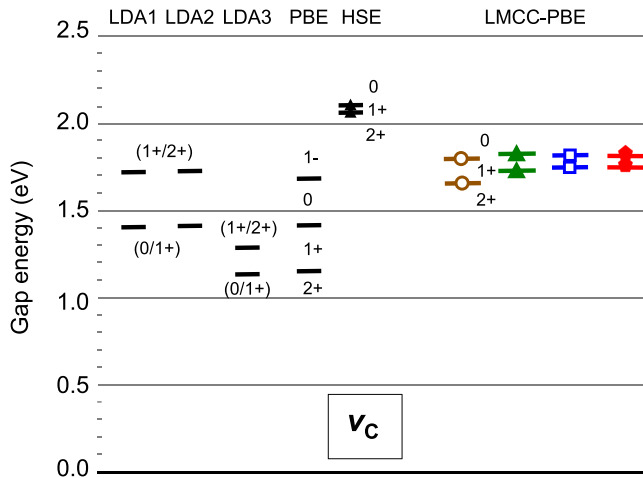


FIG. 7. Defect levels for the carbon vacancy,  $v_C$ . LDA results from Zywiets (LDA1) [5], Bechstedt (LDA2) [57], and Bockstedt (LDA3) [8], and PBE and HSE results from Oda [13] are depicted from left to right next to the current LMCC-PBE levels. System sizes for LMCC-PBE are indicated as in Fig. 6. The relaxed structure is the same for all system sizes, and the spacing of the ionization levels is well converged at 216 (green triangle) or 512 (blue square) atom supercells.

$v_C$ - $D_{2d}$  is unambiguously a deep defect (levels 0.6 and 0.7 eV below the CBE), with its Kohn-Sham states cleanly inside the Kohn-Sham band gap.

Our PBE defect levels differ from Oda's PBE results and instead resemble their HSE0.15 defect levels [13]. The  $v_C(0)$  PBE formation energies (Table IV) only differ by 0.1 eV, and we again attribute the modest differences in the defect level diagram to use of the more rigorous treatment of charged defects via the LMCC. Additionally, in the distorted  $D_{2d}$  structure, the current results exhibit no contamination with the CB [13] and thus lie deeper in the gap than the HSE0.15 results.

### 3. Divacancy - $vv$

As for the silicon vacancy,  $v_{Si}$ , the divacancy in SiC can either appear as the simple divacancy  $vv'$ , or undergo a site shift to  $vv^*$ , as shown in Fig. 8. We discuss the configurations in detail separately below. In Fig. 9, we show the thermodynamic levels for each structure separately, and then combined as that might correspond better to experimental observations.

*The simple divacancy.* The nearest-neighbor vacancy pair  $v_C$ - $v_{Si}$ , the simple divacancy  $vv'$ , has been identified as an extremely stable defect in 3C-SiC [58]. The  $vv$  has proved to be important defect in materials such as GaAs [24] where it was shown to be a prominent defect center in irradiated material. While a high absolute formation energy of the  $vv$ , 7.17 eV from Table IV, precludes any significant population in equilibrium grown material, the neutral divacancy is as stable

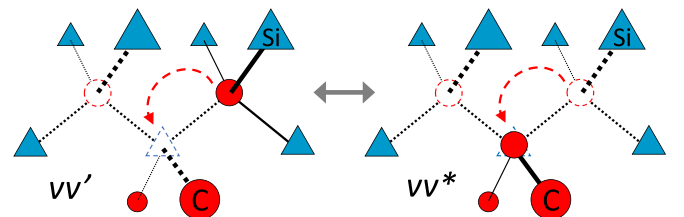


FIG. 8. Schematic depiction of the  $vv_{Si}$  bistability between the simple divacancy  $vv'$  and site-shifted divacancy  $vv^*$  ( $= v_C$ - $C_{Si}$ - $v_C$ ).

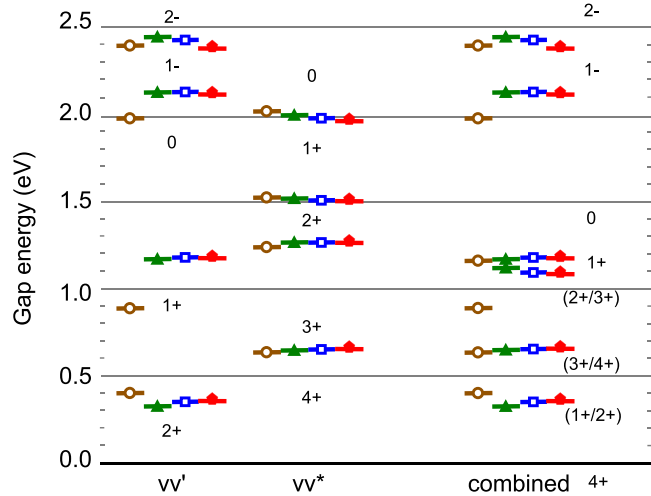


FIG. 9. Thermodynamic levels for the divacancy complex. From left to right, levels for the simple divacancy ( $vv'$ ), the site-shifted ( $vv^*$ ), and the combined levels using the lowest energy configuration for each charge state. Charge states are indicated as in Fig. 4, and LMCC system sizes as in Fig. 6.

as the simple Si vacancy, suggesting it might be a common defect in implanted/irradiated SiC.

In an early LDA study, Torpo *et al.* [58] found charge states ranging from (2+) through (2-) for  $vv'$  in 3C-SiC, contingent on the means used to incorporate finite cell electrostatic errors (the (2+) might disappear into the CB). Gordon *et al.* despite finding stable (1-) and (2-) charge states in 4H-SiC, found no stable negative charge states using the HSE functional for  $vv$  in 4C-SiC [59]. The neutral  $vv$  was claimed to be the stable charge state for Fermi levels above VB + 1.0 eV.

For the simple  $vv'$ , we find stable charge states ranging from (2+) through (2-), confirming the earlier LDA result [58]. The  $vv'(0)$  adopts a  $C_{3v}$  structure, the pair of electrons in the degenerate  $e$  doublet being triplet coupled in the ground state. The intermediate (1-) and (1+) charge states would lead to degenerate electronic configurations in  $C_{3v}$ .

Our results exhibit Jahn-Teller-induced distortions to doublet-spin  $C_{1h}$ , distortions that increased in cell size, amounting to more than 0.03 eV for the (1-) and more than 0.25 eV for (2+). The doubly charged defects are nondegenerate and remain singlet spin in a  $C_{3v}$  structure.

The 64-site supercell proved inadequate. Finite cell errors overwhelmed the correct description of the defect. The singly charged defects, rather than undergoing a Jahn-Teller distortion, collapsed to the unphysical  $C_{3v}$ . Defect state banding from the dense array of supercell defects corrupted the electronic state occupations. Despite this failure in the small 64-site cell, the results proved well-converged in just the next larger 216-site supercell.

The simple divacancy has defect levels that almost span the full SiC band gap. The  $vv'(2+ / 1+)$  is 0.36 eV above the VBE, stepping through levels at 1.18, 2.13, and ultimately to a  $vv'(1- / 2-)$  level at 2.42 eV. The KS occupied states of the latter are cleanly in the gap, separate from distinct CBE KS marker states. This  $vv'(2- / 1-)$  transition serves as the lower

bound on the location of the conduction band edge on this energy scale.

The results for this single defect refute the prevalent belief that a KS band gap problem compels a defect level band gap problem. The KS gap for PBE is only 1.33 eV, yet the range of properly referenced, total-energy-derived defect levels in  $vv'$  by itself span just over 2.1 eV. We note that the levels extrapolated using the Jost model from the 216-site supercell and the 512-site supercell almost exactly match; the largest difference is only 26 meV. This precision of agreement and fine-scale convergence is achieved from an analysis including Jost long-range screening energy contributions that are 100 times larger (see Table III). This indicates, first, that the  $vv'$ , despite failing in the 64-site supercell, is well-localized in the 216- and 512-site supercells (otherwise such convergence would be impossible) and, second, that the remaining finite cell effects are predominantly due to classical dielectric screening that is accurately approximated by the modified Jost model.

*Divacancy site shift.* The divacancy in SiC can access yet more highly charged states, down to (4+), through the site shift as depicted in Fig. 8. A neighboring carbon atom shifts into the vacated Si site to form a  $v_C-C_{Si}-v_C$  complex we denote as  $vv^*$ . While a site shift in a simple single vacancy is found to be relatively common in other compound semiconductors [22] and manifests in the  $v_{Si}$  discussed in above, it has not been documented in a divacancy.

The  $vv^*(0)$ , the highest stable site shift, has a formation energy 2.1 eV above the simple  $vv'(0)$ . As electrons are removed, however, it becomes relatively more stable very quickly, as the Si dangling bonds in the  $vv^*$  ionize more easily than the C dangling bonds in  $vv'$ . The  $vv^*(1+)$  is only 1.3 eV above the  $vv'(1+)$  and comes within <0.2 eV in the (2+) charge state.

The site-shift reconfiguration of the defect induces a negative-effective- $U$  (1+ / 3+) transition. The  $vv(2+)$  is thermodynamically unstable and the  $vv'(1+ / 2+)$  level at 0.36 disappears, subsumed into the  $-U$   $vv'(1+) / vv^*(3+)$  transition emitting two electrons at 0.72 eV above the VBE. The divacancy's final ionization is the new  $vv^*(3+ / 4+)$  level at 0.66 eV.

The full divacancy can adopt charge states ranging from (4+), in its site-shift  $vv^*$  form, to (2-) in its simple  $vv'$  form. This indicates the importance of not only fully exploring local distortions in a defect's configuration but also investigating potential site shifts in all vacancy-related defects, including divacancies.

#### 4. Silicon interstitial - $Si_i$

The silicon interstitial,  $Si_i$  has two competitive structures, previously identified as the symmetric  $C_{2v}$  split-(110) $_{Si}$  and the tetrahedral interstice with carbon near neighbors  $T_{i(C)}$  [8,9,13,60]. After an extensive search through split-(001) and -(110) configurations at both C and Si sites and  $T_{i(C)}$  and  $T_{i(Si)}$  sites, including consideration of symmetry lowering distortions, we confirm that the  $T_{i(C)}$  site (high-spin) and the  $C_{2v}$ -(110) $_{Si}$  (low-spin) are the dominant structures for Fermi levels across the band gap. We find that both configurations can take charge states from (4+) through (0), although the



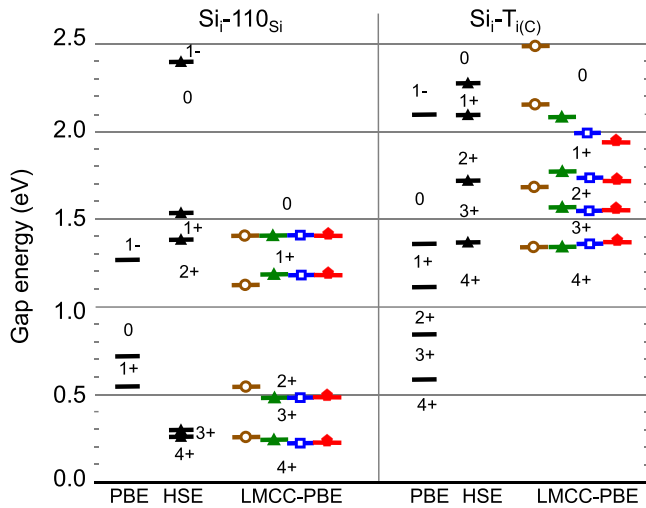


FIG. 10. The defects levels for the silicon interstitial with split configuration  $C_{2v}$ - $(110)_{Si}$  (left) and tetrahedral interstice with carbon near neighbors  $T_{i(C)}$  (right) shown as separate defects. Results using PBE and HSE by Oda [13] are shown with the LMCC-PBE results for all system sizes. Charge states are indicated as in Fig. 4 and LMCC system sizes as in Fig. 6. The full  $Si_i$  level diagram in (Fig. 4) combines these defects to traverse from the  $(110)_{Si}(0)$  through the positively charged  $T_{i(C)}$  sites.

$T_{i(C)}(0)$  is likely a shallow state. The one unanticipated result is the finding that the split-(110) (2+) defect prefers a triplet-spin state rather than the singlet, by 0.24 eV, prompted by an accidental near-degeneracy between two orbitals.

For the neutral interstitial, the two structures are close in energy, (see Table IV) with  $(110)_{Si} \sim 0.1$  eV lower in the largest supercell. The  $(110)_{Si}(0)$  formation energy converges well with larger cell size, but the  $T_{i(C)}$  site converges poorly, and gives a very bad ( $>1$  eV higher) result for the 64-site supercell. For positive charge systems, the  $T_{i(C)}$  site is favored. At (+1), it is more favorable by 0.4 eV, and the margin increases with charge state through the (4+), to 3.2 eV.

Figure 10 shows the site-resolved computed level diagrams for  $(110)_{Si}(0)$  and  $T_{i(C)}$ . As the spinless  $(110)_{Si}$  defect was used as the Jost model calibration benchmark in Fig. 3, it is little surprise that the spin-polarized  $(110)_{Si}$  exhibits near-perfect convergence with cell size here. This is a well-localized defect in all its charge states. The  $T_{i(C)}$  convergence is less good, especially for the 64-site cell, and particularly for the (0/1+) level, which changes 0.5 eV across the cell sizes. This kind of large drift in the levels can be indicative of contamination with a band edge, a notion supported by the severe error in the neutral formation energy in the 64-site cell, as shown in Table IV.

Examination of the  $T_{i(C)}(0)$  KS eigenstates does reveal potential hybridization with the CBE, not fully resolved in even the largest 1000-site supercell: the defect KS state and a shifted CBE marker state in the defect calculation bracket the CBE KS eigenstate in the perfect crystal. The Jahn-Teller-vulnerable (3+) and (2+) states show small, but clearly resolved distortions (lowering the energy 0.03 eV) that shift the interstitial along the (111)-axis, while the quartet-spin (1+) conserves a nondegenerate  $T_d$  symmetry. The triplet (0)

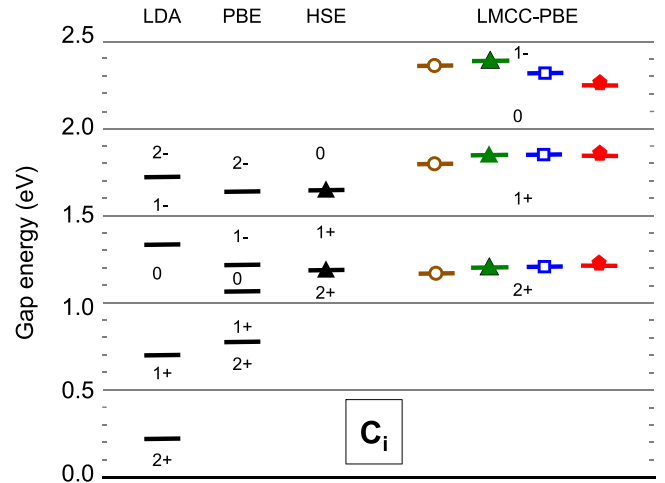


FIG. 11. Defect levels for the carbon interstitial,  $C_i$ . From left to right results are from Lento (LDA) [9], Oda (PBE and HSE) [13], and the current LMCC-PBE work. Charge states are indicated as in Fig. 4, and LMCC system sizes as in Fig. 6.

also shows a distortion, although smaller ( $<0.02$  eV relaxation), suggesting it too is a stable local state, but perhaps very shallow.

Once again, our LMCC-PBE levels for the  $T_{i(C)}$  structure resemble the levels computed with HSE more than the conventionally referenced PBE [13]. Our  $(110)_{Si}$  results exhibited good cell-size convergence and the defect KS eigenstates were cleanly resolved from the conduction band edge, unlike the contamination reported by Oda *et al.* [13]. Instead, we find that the (1-) charge state is not a stable charge state and does not lead to a level in the gap.

### 5. Carbon interstitial - $C_i$

Figure 11 shows our predicted defect levels for the carbon interstitial  $C_i$ . The LMCC-derived thermodynamic PBE defect levels traverse stable charge states from (2+) through (1-). The level structure is again similar to the HSE result from Oda *et al.* [13] with the addition of a (1-/0) state near the conduction band edge. Our results differ quantitatively from their PBE levels as well as earlier LDA calculations [9], again reflecting the more rigorous total-energy treatment offered by the LMCC boundary conditions.

The ground state for all of the  $C_i$  charge states is a  $(001)_C$ -split configuration. The (2+) adopts a symmetric  $D_{2d}$  structure. A degeneracy in the symmetric (1+) defect prompts a Jahn-Teller-like distortion to a twisted  $D_2$  structure [8], favored by 73 meV over the  $C_{1h}$  tilted- $(001)_C$  distortion. This confirms that the  $C_i(1+)$  is a viable assignment for the  $D_2$ -symmetry  $T_5$  center seen in EPR [49]. The triplet-spin  $D_{2d}(0)$  is nondegenerate and is the neutral ground state. In contrast to Bockstedte *et al.* [8], we find the twisted- $D_2$  (1-) to be in the conduction band, but instead find the tilted- $(001)_C$  to be ground state of the Jahn-Teller distorted  $C_i(1-)$ . The excellent convergence of the LMCC results with cell size illustrates the effectiveness of the classical Jost screening in evaluating the long-range screening energy in independently extrapolating each cell result to the infinitely dilute limit.

The (1−) charge state is barely in the gap. In the larger supercells, it becomes contaminated slightly with the CBE, explaining the minor drop-off with cell size for the (1−/0) level at the largest cell size. This indicates this state is right at or near the CBE, and the clean 216-site (1−/0) defect level at 2.38 eV represents a lower bound of the CBE. The positions of the other transitions differ significantly from Lento's LDA levels [9] and Oda's PBE levels [13]. This is certainly due to the LMCC boundary conditions used here. With the (1−/0) right near the band edge, we see no sign of a stable (2−) state that might give rise to the (2−/1−) seen in these other DFT studies.

While there is no stable (2−) state that leads to a (2−/1−) level in the split-(001)<sub>C</sub> structure, we do find a (just barely) stable (2−) in the split-(001)<sub>Si</sub> configuration. This (2−) charge state is not thermodynamically accessible [it would spontaneously emit an electron and reconfigure to the (001)<sub>C</sub> (1−) structure]. Its direct ionization to (001)<sub>Si</sub> (1−) leads to a level at 2.39 eV, and provides yet another confirmation on the bound on the CBE.

### 6. Carbon antisite - C<sub>Si</sub>

We find the carbon antisite C<sub>Si</sub> (the isoelectronic carbon replacing a silicon atom in the lattice) retains the  $T_d$  symmetry of the site and has no levels in the band gap. Only the neutral charge state is stable. This result is in agreement with Torpo *et al.* [4].

The smaller carbon atom induces a significant 12% contraction in the bond length to its carbon neighbors. Despite this strong contraction, the formation energy is well converged in even the small 64-atom supercell; the elastic finite size cell error is surprisingly small.

The relatively low formation energy for the neutral defect, 3.67 eV (see Table IV), is nonetheless high enough that few will be present in equilibrium grown material. Being chemically and electronically inert, the defect is technologically unimportant, except perhaps as a secondary defect that acts as an invisible sink in radiation-damaged material.

### 7. Silicon antisite - Si<sub>C</sub>

The silicon antisite Si<sub>C</sub> (isoelectronic silicon replacing a carbon in the lattice) is complicated [4], and our analysis is not entirely conclusive in even the largest 1000-atom supercells.

The Si<sub>C</sub>(0) remains  $T_d$ , with bonds to the neighboring Si diluted by 14% with respect to the perfect lattice. This 2.16-Å Si-Si bond distance leaves the antisite Si-Si bonds strongly compressed (9%) with respect to the ideal 2.37-Å Si-Si bond distance (for bulk PBE silicon). The formation energy (see Table IV) converges well with supercell size, although less well than for the carbon antisite. The 64-site supercell silicon antisite is almost 0.2 eV higher than the converged supercell result, highlighting the impaired reliability of this small supercell. The severe compression in the antisite bonds pushes a triplet of degenerate states 0.19 eV above the Kohn-Sham VB, and the silicon antisite therefore acts as a donor. The challenge becomes, theoretically, to resolve how many of these six electrons in the  $p$ -like states ultimately can be extracted from the defect before the remaining electron states are pulled below the VBE.

The (1+) antisite is unambiguously a stable charge state, with its KS eigenstates cleanly inside the KS band gap. In the  $T_d$  structure, the ionized defect would leave a triply degenerate state. We resolve a distortion to a  $C_{2v}$  structure for the Si<sub>C</sub>(1+). The positive antisite atom shifts slightly off-center resulting in two slightly shorter 2.17-Å bonds and two longer 2.20-Å bonds to its neighbors. This distortion is already established in the small 64-atom supercell and strengthens slightly into the larger volume afforded by the larger supercells. The total energy lowering from the  $T_d$  (including spin polarization) is 30–40 meV, again well converged in even the smallest supercell.

The (0/1+) defect level converges well, to 0.65 eV above the VBE. We point out this level is significantly different from the KS scale, where the defect eigenstate at only 0.19 eV above the VBE. This confirms the quantitative disconnect between the total-energy-derived defect levels and defect KS state eigenvalues documented in the Ga antisite in GaAs [29], where the properly referenced total energy calculations led to levels that were expanded from the energy scale given by the KS eigenvalues.

A second ionization to form the  $T_d(2+)$  still leaves the defect KS eigenstates distinctly, if only slightly (0.05 eV), above a set of KS eigenstates that can be cleanly associated with the crystal VBE eigenstates. A significant spin polarization energy (to a triplet) testifies to the continued locality in this charge state, but this spin polarization shrinks with cell size, from 0.10 eV in the small cell to 0.03 eV in the 1000-atom supercell. A small structural distortion in response to the Jahn-Teller degeneracy is likely present, but amounts to less than 20 meV, and cannot be cleanly resolved.

The third and fourth ionization become further delocalized in these discriminating probes of locality [29]. However, a distinct, seemingly unperturbed VBE marker eigenstate persists with the defect eigenstates above it. It is only with the removal of a fifth electron that the defect KS eigenstate clearly sinks below the VBE marker eigenstate. This stability of the antisite from the neutral to the (4+) charge state matches the early LDA result of Torpo *et al.* [4]. These deeper ionizations remain in the band gap, but lack the unambiguous signatures used to discriminate deep states from shallow states in GaAs [29]. This suggests that these highly charged states in SiC are likely shallow states.

Figure 12 shows the Si<sub>C</sub> levels as function of supercell. The computed levels reflect the analysis depicted above. The (0/1+) level is cleanly a deep defect, converged at even the smallest cells size, to  $\gtrsim 0.6$  eV above the VBE. The (1 + /2+) level also converges cleanly in larger cells, to  $\sim 0.4$  eV. The deeper transitions, however, are still shifting strongly and not fully converged at even at the largest cell sizes, consistent with a weak localization associated with a shallow transition. Our spin-polarized PBE levels in these large supercells are roughly consistent with earlier LDA results. Torpo *et al.* [4] had associated their LDA antisite levels with the  $H1$ ,  $H2$ , and  $H3$  hole traps seen by Nagesh *et al.* [61] in DLTS (deep level transient spectroscopy) experiments. It is not clear that these traps correspond to the same defect, as they have different annealing behavior but, particularly given that the  $H2$  trap was noted to possibly encompass two different levels, it is very tempting to assign the four transitions of the Si antisite

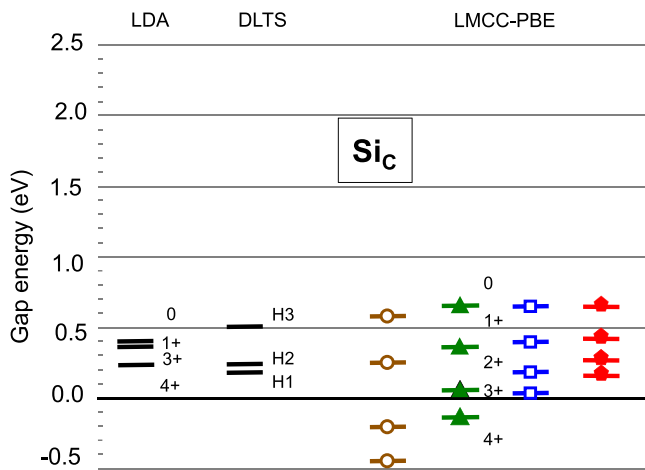


FIG. 12. Defect levels for the silicon antisite  $\text{Si}_C$ . From left to right are results from Torpo (LDA) [4], using a 128 atom supercell, experimental DLTS results from Nagesh (DLTS) [61], and the current LMCC-PBE work. Charge states are indicated as in Fig. 4, and LMCC system sizes as in Fig. 6. The DLTS results do not have unambiguously identified charge transitions, are identified only as  $H1$ ,  $H2$ , and  $H3$ . The LMCC results clearly show that the smaller supercells are not reliable for this defect, with higher charge states disappearing into the VB for systems smaller than 512 atoms.

to these trap states. The accuracy in assigning the antisite levels to the  $H1$ - $H2$ - $H3$  traps would be consistent with the typical accuracy ( $<0.2$  eV) obtained using LMCC methods for computed defect levels in Si [20] and GaAs [24].

### 8. Di-antisite - $\text{Si}_C\text{C}_{\text{Si}}$

A diantisite is a common defect in radiation-damaged materials, the consequence of sequential knock-ons channeled along a (111) axis. Like the single antisites, the switch of the C and Si along the bond creates an atomic configuration isoelectronic with the undefected crystal. The diantisite results very closely parallel the silicon antisite, exhibiting stable charge states from (0) to (4+). The defect levels, with almost identical level positions and almost identical cell-size dependence, yield almost the identical defect levels diagram for  $\text{Si}_C$  depicted in Fig. 12 and would be experimentally indistinguishable from the silicon antisite.

## V. DISCUSSION

The current results, despite a formal KS band gap problem, show better alignment with the hybrid functional results [13] than nominally equivalent PBE results using a jellium neutralization [13]. The principal reason for the difference between our and previous DFT studies in  $3C$ -SiC is that conventional jellium-based approaches are unable to properly reference charge states in supercell calculations. Given the close similarities between HSE and PBE defect calculations in Oda [13], with geometries and electron densities nearly identical, the two approaches must follow nearly identical potential energy surfaces. That their inferred energy for levels differed so greatly indicates the importance of treating long-range screening, and referencing to a perfect crystal potential.

The close parallel of HSE and our LMCC-PBE results in most cases is evidence that the PBE and HSE give similar defect results regardless of the nominal KS band gap.

In many comparisons to previous DFT results above, the differences can be ascribed partially to the use of the small supercells in older computational studies. Our analysis of finite cell dependence indicates  $O(100)$ -site supercells are qualitatively unreliable, that 216-site supercells are the minimum needed to get a qualitatively reliable result, and that 512-site supercells are the minimum needed to verify quantitative convergence. Moreover, there exist defects, especially near band edges, that are not resolved even with large 1000-site supercells. This observation documents that it is crucial to perform finite-cell convergence tests in any DFT defect study, even in wide band gap materials such as SiC, to make predictions of defect character or the defect levels with any confidence.

We reiterate that the cell size convergence observed in these results is not the result of rescaling to an experimental band gap or re-referencing to KS eigenvalues, but are the results of total energy differences that have no information about, or referencing to, band edges, either experimental or Kohn-Sham eigenstates. The typical 10–20 meV agreement between the levels computed for the 512-site and 1000-site cells emerges naturally with long-range screening contributions up to 10 eV (Table III). This resolution is of order 1 part in 1000 of the long-range classical screening energy, testimony both to the convergence of the finite-cell results, and to the effectiveness of the modified Jost model to accurately evaluate long-range screening effects in finite size supercell calculations.

## VI. CONCLUSION

We have presented a detailed analysis of defect structures and energies for an extensive set of intrinsic defects in  $3C$ -SiC. This analysis is grounded in a systematic assessment and understanding of finite cell effects, documented to be converged to infinitely dilute bulk limit and using rigorous boundary conditions that are demonstrated to not manifest a band gap problem in the computed defect levels.

We quantify the widely unappreciated magnitude of long-range screening energy in finite cell supercells (almost 8 eV even in the largest 1000-site supercells, more than three times the band gap) and demonstrate the validity and effectiveness of a simple modified Jost model to incorporate the long-range classical dielectric screening outside the volume defined by the supercell. The fine scale cell-size convergence, few  $10$ 's of meV, between the results between the largest supercells, across almost the entire set of computed defect levels including this large empirical term, testifies to the robustness of an approach that takes rigorous and explicit account of electrostatic boundary conditions in charged supercells using the LMCC approach.

We tested for finite size errors and assess convergence of the calculations to the infinite bulk limit in supercell calculations that range from small 64 atom supercells through 1000-atom supercells. Supercells below 216 sites are shown to give results that are qualitatively unreliable, while the results are shown to converge very well with larger supercells.

This demonstrates the necessity of using larger supercells to get reliable results, and of yet larger supercells to verify convergence to a bulk limit. We expect that similar scale supercells will be needed, and be sufficient, for investigations of defects in other SiC polytypes, e.g., the technologically relevant *4H*-SiC where size-scaling verification studies are more problematic.

The silicon vacancy had long been an unresolved mystery, in particular, the  $v_{\text{Si}}(0)$  had inspired hypotheses of exotic behavior not exhibited in other SiC defects. The results here showed that the singlet-spin  $T_d$  structures that were superior to the triplet-spin  $T_d$ , are inferior to a triplet-spin distortion to a reduced symmetry  $C_{3v}$  structure, and that the other viable charge states of the simple vacancy that showed Jahn-Teller degeneracies also proved unstable to symmetry-lowering distortions.

The simple divacancy in SiC, touted as a possible candidate as an optically active spin qubit center [62], was shown to have an unprecedented site-shift bistability that would dominate in *p*-type materials, similar to the  $v_{\text{Si}}$ , and adds a new unanticipated wrinkle that needs to be considered in future studies. These benchmark defect results in the *3C*-SiC will be invaluable to inform investigations of the analogous defects in the more common polytypes such as *4H*-SiC.

The nominal KS band gap problem of PBE (and LDA) proved not be a problem for defects in *3C*-SiC. In fact, the effective defect band gap, defined as the span of valid localized defect transitions computed across all defects, was found to match the experimental band gap very closely. The PBE defect levels computed here showed closer alignment with good quality (216-site) empirically tailored hybrid functional defect levels [13] than with any earlier DFT levels computed lacking

rigorous control of the boundary conditions. The lingering question this poses, however, is: given the evidence presented here that a careful treatment of charge boundary conditions is crucial to get a good description of defect levels, how does a jellium-based hybrid functional approach do as well lacking any such rigor in the electrostatics?

## ACKNOWLEDGMENTS

We thank Richard Dobzynski (U. Virginia) for assistance in the bulk SiC calculations. We express our gratitude to Andrew Pineda (Air Force Research Laboratory) for assistance in mounting the large scale parallel calculations. We are grateful to Andrew Mounce for useful conversations, and to Jesse Lutz for a critical reading of the manuscript. Sandia National Laboratories is a multimission laboratory managed and operated by National Technology and Engineering Solutions of Sandia, LLC., a wholly owned subsidiary of Honeywell International, Inc., for the US Department of Energy's National Nuclear Security Administration under Contract No. DE-NA0003525. This work (Sandia) was supported by a Laboratory Directed Research and Development (LDRD) project, and was funded, in part, at the Center for Integrated Nanotechnologies, an Office of Science User Facility operated for the US Department of Energy (DOE) Office of Science. AFRL gratefully acknowledges the support of the Air Force Office of Scientific Research (AFOSR) through Contract No. FA9550-17RVCOR505. This paper describes objective technical results and analysis. Any subjective views or opinions that might be expressed in the paper do not necessarily represent the views of the US Department of Energy or the United States Government.

- 
- [1] J. B. Casady and R. W. Johnson, Status of silicon carbide (SiC) as a wide-bandgap semiconductor for high-temperature applications: A review, *Solid State Electron.* **39**, 1409 (1996).
  - [2] M. Syväjärvi, Q. Ma, V. Jokubavicius, A. Galeckas, J. Sun, X. Liu, M. Jansson, P. Wellmann, M. Linnarsson, P. Runde, B. A. Johansen, A. Thøgersen, S. Diplas, P. A. Carvalho, O. M. Løvvik, D. N. Wright, A. Y. Azarov, and B. G. Svensson, Cubic silicon carbide as a potential photovoltaic material, *Sol. Energy Mater. Sol. Cells* **145**, 104 (2016).
  - [3] C. Wang, J. Bernholc, and R. F. Davis, Formation energies, abundances, and the electronic structure of native defects in cubic SiC, *Phys. Rev. B* **38**, 12752 (1988).
  - [4] L. Torpo, S. Pöykkö, and R. M. Nieminen, Antisites in silicon carbide, *Phys. Rev. B* **57**, 6243 (1998).
  - [5] A. Zywiets, J. Furthmüller, and F. Bechstedt, Vacancies in SiC: Influence of Jahn-Teller distortions, spin effects, and crystal structure, *Phys. Rev. B* **59**, 15166 (1999).
  - [6] G. Cubiotti, Y. Kucherenko, A. Yaresko, A. Perlov, and V. Antonov, The effect of the atomic relaxation around defects on the electronic structure and optical properties of  $\beta$ -SiC, *J. Phys. Condens. Matter* **11**, 2265 (1999).
  - [7] P. Deák, J. Miró, A. Gali, L. Udvardi, and H. Overhof, The spin state of the neutral silicon vacancy in *3C*-SiC, *Appl. Phys. Lett* **75**, 2103 (1999).
  - [8] M. Bockstedte, A. Mattausch, and O. Pankratov, *Ab initio* study of the migration of intrinsic defects in *3C*-SiC, *Phys. Rev. B* **68**, 205201 (2003).
  - [9] J. M. Lento, L. Torpo, T. E. M. Staab, and R. M. Nieminen, Self-interstitials in *3C*-SiC, *J. Phys.: Condens. Matter* **16**, 1053 (2004).
  - [10] J. Isoya, T. Umeda, N. Mizuochi, N. T. Son, E. Janzén, and T. Oshima, EPR identification of intrinsic defects in SiC, *Phys. Status Solidi b* **245**, 1298 (2008).
  - [11] F. Bruneval and G. Roma, Energetics and metastability of the silicon vacancy in cubic SiC, *Phys. Rev. B* **83**, 144116 (2011).
  - [12] F. Bruneval, Methodological aspects of the GW calculation of the carbon vacancy in *3C*-SiC, *Nucl. Instrum. Methods Phys. Res. B* **277**, 77 (2012).
  - [13] T. Oda, Y. Zhang, and W. J. Weber, Study of intrinsic defects in *3C*-SiC using first-principles calculation with a hybrid functional, *J. Chem. Phys.* **139**, 124707 (2013).
  - [14] L. Torpo, R. M. Nieminen, K. E. Laasonen, and S. Pöykkö, Silicon vacancy in SiC: A high-spin state defect, *Appl. Phys. Lett.* **74**, 221 (1999).
  - [15] A. Zywiets, J. Furthmüller, and F. Bechstedt, Spin state of vacancies: From magnetic Jahn-Teller distortions to multiplets, *Phys. Rev. B* **62**, 6854 (2000).



- [16] G. Makov and M.C. Payne, Periodic boundary conditions in *ab initio* calculations, *Phys. Rev. B* **51**, 4014 (1995).
- [17] T. Oda, Y. Zhang, and W. J. Weber, Optimization of a hybrid exchange-correlation functional for silicon carbides, *Chem. Phys. Lett.* **579**, 58 (2013).
- [18] P. A. Schultz, Local electrostatic moments and periodic boundary conditions, *Phys. Rev. B* **60**, 1551 (1999).
- [19] P. A. Schultz, Charged Local Defects in Extended Systems, *Phys. Rev. Lett.* **84**, 1942 (2000).
- [20] P. A. Schultz, Theory of Defect Levels and the “Band Gap Problem” in Silicon, *Phys. Rev. Lett.* **96**, 246401 (2006).
- [21] R. M. Van Ginhoven and P. A. Schultz, Off-center TI and Na dopant centers in CsI dopant centers in CsI, *J. Phys.: Condens. Matter* **25**, 495504 (2013).
- [22] P. A. Schultz and O. A. von Lillienfeld, Simple intrinsic defects in gallium arsenide, *Modelling Simul. Mater. Sci. Eng.* **17**, 084007 (2009).
- [23] P. A. Schultz and A. H. Edwards, Modeling charged defects inside density functional theory band gaps, *Nucl. Instrum. Methods Phys. Res. B* **327**, 2 (2014).
- [24] P. A. Schultz, The  $E1-E2$  center in gallium arsenide is the divacancy, *J. Phys.: Condens. Matter* **27**, 075801 (2015).
- [25] P.A. Schultz, SEQQUEST code (unpublished), see <https://dft.sandia.gov/Quest/>.
- [26] D. R. Hamann, Generalized norm-conserving pseudopotentials, *Phys. Rev. B* **40**, 2980 (1989).
- [27] J. P. Perdew and A. Zunger, Self-interaction correction for density-functional approximations for many-electron systems, *Phys. Rev. B* **23**, 5048 (1981).
- [28] J. P. Perdew, K. Burke, and M. Ernzerhof, Generalized Gradient Approximation Made Simple, *Phys. Rev. Lett.* **77**, 3865 (1996).
- [29] P. A. Schultz, Discriminating a deep gallium antisite defect from shallow acceptors in GaAs using supercell calculations, *Phys. Rev. B* **93**, 125201 (2016).
- [30] J. Lento, J.-L. Mozos, and R. M. Nieminen, Charged point defects in semiconductors and the supercell approximation, *J. Phys.: Condens. Matter* **14**, 2637 (2002).
- [31] W. Jost, Diffusion and electrolytic conduction in crystals (ionic semiconductors), *J. Chem. Phys.* **1**, 466 (1933).
- [32] L. Patrick and W. J. Choyke, Static dielectric constant of SiC, *Phys. Rev. B* **2**, 2255 (1970).
- [33] M. A. Anders, P. M. Lenahan, A. H. Edwards, P. A. Schultz, and R. M. Van Ginhoven, Effects of nitrogen on the interface density of states distribution in 4H-SiC metal oxide semiconductor field effect transistors: Superhyperfine interactions and near interface silicon vacancy energy levels, *J. Appl. Phys.* **124**, 184501 (2018).
- [34] W. R. L. Lambrecht, B. Segall, M. Methfessel, and M. van Schilfhaarde, Calculated elastic constants and deformation potentials of cubic SiC, *Phys. Rev. B* **44**, 3685 (1991).
- [35] K. Karch, P. Pavone, W. Windl, O. Schütt, and D. Strauch, *Ab initio* calculations of structural and lattice-dynamical properties of silicon carbide, *Phys. Rev. B* **50**, 17054 (1994).
- [36] S. Hu, W. Setyawan, R. M. Van Ginhoven, W. Jiang, C. H. Henager, Jr., and R. J. Kurtz, Thermodynamic and kinetic properties of intrinsic defects and Mg transmutants in 3C-SiC determined by density functional theory, *J. Nucl. Mater.* **448**, 121 (2014).
- [37] L. Pizzagalli, Stability and mobility of screw dislocations in 4H, 2H and 3C silicon carbide, *Acta Mater.* **78**, 236 (2014).
- [38] D. W. Feldman, J. H. Parker, Jr., W. J. Choyke, and L. Patrick, Phonon dispersion curves by Raman scattering in SiC, polytype 3C, 4H, 6H, 15R, and 21R, *Phys. Rev.* **173**, 787 (1968).
- [39] P. Djemia, Y. Roussigné, G. F. Dirra, and K. M. Jackson, Elastic properties of  $\beta$ -SiC films by Brillouin light scattering, *J. Appl. Phys.* **95**, 2324 (2003).
- [40] Z. Li and R. C. Bradt, Thermal expansion of the cubic (3C) polytype of SiC, *J. Mater. Sci.* **21**, 4366 (1986).
- [41] R. H. Rein and J. Chipman, The free energy of SiC from its solubility in Fe from gas-solid equilibria with SiO<sub>2</sub> graphite and CO, *J. Phys. Chem.* **67**, 839 (1963).
- [42] C. Persson and U. Lindefelt, Relativistic band structure calculation of cubic and hexagonal SiC polytypes, *J. Appl. Phys.* **82**, 5496 (1997).
- [43] R. G. Humphreys, D. Bimberg, and W. J. Choyke, Wavelength modulated adsorption in SiC, *Solid State Commun.* **39**, 163 (1981).
- [44] C. H. Park, B.-H. Cheong, K.-H. Lee, and K. J. Chang, Structural and electronic properties of cubic, 2H, 4H, and 6H SiC, *Phys. Rev. B* **49**, 4485 (1994).
- [45] C. Persson and U. Lindefelt, Detailed band structure for 3C-, 2H-, 4H-, 6H-SiC, and Si around the fundamental band gap, *Phys. Rev. B* **54**, 10257 (1996).
- [46] S. B. Zhang and J. E. Northrup, Chemical potential dependence of defect formation energies in GaAs: Application to Ga self-diffusion, *Phys. Rev. Lett.* **67**, 2339 (1991).
- [47] P. A. Burr and M. W. D. Cooper, Importance of elastic finite-size effects: Neutral defects in ionic compounds, *Phys. Rev. B* **96**, 094107 (2017).
- [48] See Supplemental Material at <http://link.aps.org/supplemental/10.1103/PhysRevB.103.195202> for cell size dependence for all defects.
- [49] H. Itoh, A. Kawasuso, T. Ohshima, M. Yoshikawa, I. Nishiyama, S. Tanigawa, S. Misawa, H. Okimura, and S. Yoshida, Intrinsic defects in cubic silicon carbide, *Phys. Stat. Sol. (a)* **162**, 173 (1997).
- [50] N. T. Son, E. Sörman, W. M. Chen, C. Hallin, O. Kordina, B. Monemar, E. Janzén, and J. L. Lindström, Optically detected magnetic resonance studies of defects in electron-irradiated 3C SiC layers, *Phys. Rev. B* **55**, 2863 (1997).
- [51] J. Lefevre, J.-M. Costantini, D. Gourier, S. Esnouf, and G. Petite, Characterization of a silicon-related defect detected by its excited triplet state in electron-irradiated 3C-SiC, *Phys. Rev. B* **83**, 075201 (2011).
- [52] E. Rauls, T. Lingner, Z. Hajnal, S. Greulich-Weber, T. Frauenheim, and J.-M. Spaeth, Metastability of the neutral silicon vacancy in 4H-SiC, *Phys. Stat. Sol. (b)* **217**, R1 (2000).
- [53] M. Bockstedte, M. Heid, and O. Pankratov, Signature of intrinsic defects in SiC: *Ab initio* calculations of hyperfine tensors, *Phys. Rev. B* **67**, 193102 (2003).
- [54] R. M. Van Ginhoven, A. Chartier, C. Meis, W. J. Weber, and L. R. Corrales, Theoretical study of helium insertion and diffusion in 3C-SiC, *J. Nucl. Mater.* **348**, 51 (2006).
- [55] G. D. Watkins and J. R. Troxell, Negative-U Properties for Point Defects in Silicon, *Phys. Rev. Lett.* **44**, 593 (1980).

- [56] F. Bechstedt, A. Zywietz, and J. Furthmüller, Carbon vacancy in SiC: A negative- $U$  system, *Europhys. Lett.* **44**, 309 (1998).
- [57] F. Bechstedt, A. Fissel, J. Furthmüller, U. Grossner, and A. Zywietz, Native defects and complexes in SiC, *J. Phys. Condens. Matter* **13**, 9027 (2001).
- [58] L. Torpo, T. E. M. Staab, and R. M. Nieminen, Divacancy in 3C- and 4H-SiC: An extremely stable defect, *Phys. Rev. B* **65**, 085202 (2002).
- [59] L. Gordon, A. Janotti, and C. G. Van de Walle, Defects as qubits in 3C- and 4H-SiC, *Phys. Rev. B* **92**, 045208 (2015).
- [60] T. Liao, G. Roma, and J. Wang, First-principles study of neutral silicon interstitials in 3C- and 4H-SiC, *Phil. Mag.* **89**, 2271 (2009).
- [61] V. Nashesh, J. W. Farmer, R. F. Davis, and H. S. Kong, Defects in cubic SiC on Si, *Radiat. Eff. Defects Solids* **112**, 77 (1990).
- [62] N. T. Son, C. P. Anderson, A. Bourassa, K. C. Miao, C. Babin, M. Widmann, M. Niethammer, J. Ul Hassan, N. Morioka, I. G. Ivanov, F. Kaiser, J. Wrachtrup, and D. D. Awschalom, Developing silicon carbide for quantum spintronics, *Appl. Phys. Lett.* **116**, 190501 (2020).